



---

*Research article*

## **Optimal strategies of oncolytic virus-bortezomib therapy via the apoptotic, necroptotic, and oncolysis signaling network**

**Donggu Lee<sup>1</sup>, Aurelio A. de los Reyes V<sup>2,3</sup> and Yangjin Kim<sup>1,\*</sup>**

<sup>1</sup> Department of Mathematics, Konkuk University, Seoul, Republic of Korea

<sup>2</sup> Institute of Mathematics, University of the Philippines Diliman, Quezon City 1101, Philippines

<sup>3</sup> Biomedical Mathematics Group, Pioneer Research Center for Mathematical and Computational Sciences, Institute for Basic Science, Daejeon 34126, Republic of Korea

\* **Correspondence:** Email: [ahyouhappy@konkuk.ac.kr](mailto:ahyouhappy@konkuk.ac.kr); Tel: +82024500450; Fax: +82024581952.

**Abstract:** Bortezomib and oncolytic virotherapy are two emerging targeted cancer therapies. Bortezomib, a proteasome inhibitor, disrupts protein degradation in cells, leading to the accumulation of unfolded proteins that induce apoptosis. On the other hand, virotherapy uses genetically modified oncolytic viruses (OVs) to infect cancer cells, trigger cell lysis, and activate anti-tumor response. Despite progress in cancer treatment, identifying administration protocols for therapeutic agents remains a significant concern, aiming to strike a balance between efficacy, minimizing toxicity, and administrative costs. In this work, optimal control theory was employed to design a cost-effective and efficient co-administration protocols for bortezomib and OVs that could significantly diminish the population of cancer cells via the cell death program with the NF $\kappa$ B-BAX-RIP1 signaling network. Both linear and quadratic control strategies were explored to obtain practical treatment approaches by adapting necroptosis protocols to efficient cell death programs. Our findings demonstrated that a combination therapy commencing with the administration of OVs followed by bortezomib infusions yields an effective tumor-killing outcome. These results could provide valuable guidance for the development of clinical administration protocols in cancer treatment.

**Keywords:** oncolytic virus; bortezomib; mathematical model; optimal control theory

---

### **1. Introduction**

Cancer is characterized by abnormal cell growth and several steps of genetic mutations. Glioblastoma multiforme (GBM), a type of brain tumor, is one of the most fatal human cancers, with a low survival rate attributed to its aggressive growth and rapid, pervasive brain invasion [1,2]. Despite recent progress in cancer treatment, toxicity and corresponding side effects such as cancer-related cognitive

changes [3, 4] are common in conventional anticancer therapies such as chemotherapy and radiation therapy. Targeted cancer therapy, a promising choice with recent advances, can be a great way of eradicating cancer cells by controlling its dynamics and players in the signaling pathways that enable tumor growth [5]. Thus, there is a need for optimal control of promotion or inhibition of these intracellular molecules in cancer treatment including chemo- and oncolytic virus (OV) therapies.

The ubiquitin–proteasome system within a cell regulates the degradation of proteins, thus controlling cellular function and maintaining homeostasis [6, 7]. Therefore, proteasome inhibitors can be used to treat cancer due its inhibition of cancer cells's increased need of protein synthesis and degradation in cancer progression [6, 8]. By interfering with appropriate degradation and recycling of proteins, a critical component for cell viability [9], proteasome inhibitors induce accumulation of ubiquitin-tagged proteins, resulting in endoplasmic reticulum (ER) stress [10] and, thus, *apoptosis*, i.e., programmed cell death, of cancer cells. Bortezomib, the first proteasome inhibitor agent in cancer treatment [11], was approved for multiple myeloma and lymphoma by Food and Drug Administration (FDA) [6]. Despite minimal undesirable side effects such as accumulation of anti-apoptotic proteins, bortezomib was shown to consistently overcome the well-known apoptotic resistance of cancer cells such as melanoma cells [12], especially when combined with other anti-cancer agents [7, 13, 14].

NF $\kappa$ B, a master regulator that controls inflammation and immune responses as well as cell proliferation, stays usually in an inactive mode by its suppressor, I $\kappa$ B [15]. Various regulators such as ER stress can activate NF $\kappa$ B by degrading I $\kappa$ B which induces the translocation of NF $\kappa$ B to the nucleus and subsequent activation of various key genes, including the anti-apoptotic gate keeper, Bcl2 and suppression of the final apoptosis gene *BAX* (Figure 1) [16–20]. While the systemic homeostasis can be maintained by this production of I $\kappa$ B and the feedback control loop in normal tissue [21], a poor management of NF $\kappa$ B by I $\kappa$ B, or a constitutively active NF $\kappa$ B state, can allow the critical resistance of tumor cells to conventional anti-cancer therapy [22–26]. Therefore, agents targeting BAX showed a great potential of killing cancer cells by up-regulating BAX, thus, inducing apoptosis [17, 27]. While *apoptosis* is a typical cell death program, *necroptosis* is another form of cell death process that is caspase-independent and causes massive cell killing. This is executed by up-regulation of reactive oxygen species (ROS) from activated RIP1, a receptor-interacting-protein kinase [28]. RIP1, a key activator of necroptosis, is not involved in the apoptotic signaling pathway [28, 29]. Up-regulation of both Bcl2 and RIP1 as well as down-regulation of caspase-8 were associated with necroptosis in glioma cancer cells [30].

An emerging treatment option with rapid advances for cancer patients is oncolytic virotherapy (OV) that uses various forms of cancer-lysing viruses as a targeted therapy [31–33]. OVs can target and kill cancer cells by infection and destruction of cell structure while avoiding unnecessary damages to normal cells in tumor microenvironment (TME) [34, 35]. While these viruses can be eliminated by the immune system on the way to the target tumor [36], the high degree of replications within a cancer cell and boosting effect of OV-induced immune activities within TME [31, 37] can compensate the loss by immune cells, which enables these viruses to spread throughout the tumor from the infected tumoral region [38]. Clinical trials for various types of OVs as well as combination therapies have been conducted and are under way to test their anti-tumor efficacy and safety [6, 31, 39]. Some of them were approved by FDA for clinical use, for instance, T-Vec, a modified herpes simplex virus 1 (oHSV), for melanoma patients [6, 37, 40]. However, virus clearance due to OV-induced immunity prevents an OV therapy from efficient anti-tumor efficacy [41]. Combination therapies including OVs were suggested as an alternative method to overcome this low efficacy and several chemotherapeutic candidates are

being tested for synergistic impact on cancer cell killing [37,42].

Yoo et al. [6] demonstrated that bortezomib was not only effective in killing cancer cells but promotes synergistic anti-tumor efficacy by inducing unfolded protein response in cancer cells, which then leads to the nuclear localization of the oHSV and a significant increase in viral replication. A follow-up study [43] then showed that the OV-bortezomib combination therapy can induce necroptosis through stimulation of the secretion of various cytokines associated with inflammation. While bortezomib treatment alone initiated a typical apoptosis, the combination treatment induced necroptosis by diverting to different signaling pathways [20,44]. Kim et al. [45] developed a mathematical model of the nonlinear dynamics of complex interactions between cancer cells and immune cells in OV–bortezomib therapy based on the experimental observations including those reported in [6,43]. It was found that both injection of exogenous natural killer (NK) cells and deletion of endogenous NK cells can lead to better anti-tumor efficacy, illustrating the complex role of TME such as immune cells in regulation of dynamics of OV-tumor interaction in a combination anti-cancer therapy. In a follow-up study [46], Kim et al. investigated the intracellular signaling pathway that governs the cancer cell death mechanism in response to various levels of bortezomib with OV therapy. Anti-apoptosis status and two different cellular death mechanisms, i.e., apoptosis and necroptosis in response to bortezomib treatment, were characterized by up- or down-regulation of three key intracellular molecules (NF $\kappa$ B/Bcl2, BAX, RIP1) [46], which was consistent with experimental observations [6,20,43–45]. These works [45–47] showed that the treatment protocols significantly affect the anti-tumor efficacy in the combination therapy and illustrated the importance of the detailed analysis of both apoptotic and necroptotic death of cancer cells in bortezomib-OV therapies. Various types of mathematical models by other groups have been developed for oncolytic virus therapy [48–58] and bortezomib treatment [59–61] in various cancers.

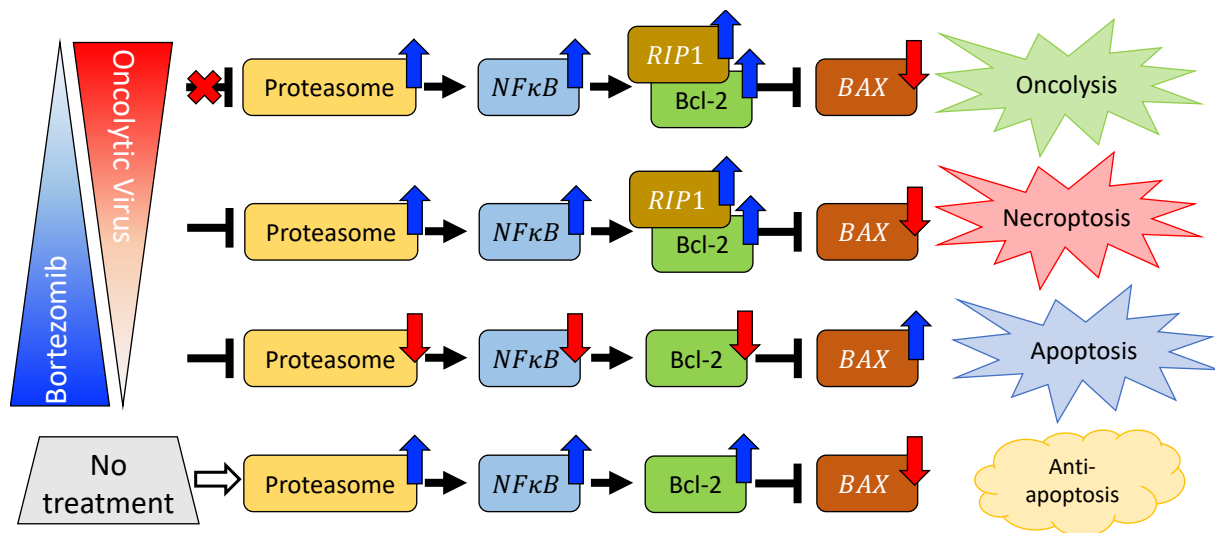


**Figure 1.** A schematic diagram depicting the role of bortezomib and OV in the regulation of cell death pathways. A minimal concentration of bortezomib combined with a robust amount of oncolytic virus (OV) synergistically drive potent oncolysis. Intermediate quantities of both bortezomib and OV promote necroptosis. Elevated bortezomib levels coupled with a limited OV presence trigger apoptosis. Conversely, scant levels of both bortezomib and OV collaboratively foster an anti-apoptotic environment.

In this study, we employ a modified mathematical model of bortezomib-OV cancer therapy, integrating cell-death pathways based on Kim et al. [46]. This refined model enables the design of optimally controlled treatment strategies. Our modeling framework utilizes *optimal control theory*, a mathematical tool that deals with complex biological systems that can be controlled by an external agent [62]. Optimal control theory has been used to determine effective administration schedules of anti-cancer agents in various cancer types [63–67] including brain tumors [47, 68–71] and lung cancers [72, 73]. For example, an optimal control method was utilized to prevent aggressive glioma cell invasion by up-regulating miR-451 [71] and controlling cell cycle [70] within cancer cells, or to optimize the anti-tumor efficacy in a nonlinear immune microenvironment [47]. Optimal control theory along mathematical models was used in various fields including epidemiology for COVID-19 [74] and MERS [75] and cancer research. In particular, optimal control scheme was used to construct cost-effective therapy protocols against cancer development, from earlier works [64–66] to recent works [76]. These studies investigated the optimal strategies in controlling tumor growth under various treatments (chemotherapy [64–66, 69, 76–78], immunotherapy [79–82], and review [63] by minimizing the tumor size and costs. In previous studies [45, 46], authors investigated the nonlinear dynamics of NK cells in a combination therapy (OVs + bortezomib) as well as anti-tumor efficacy via the intracellular signaling pathway (NF $\kappa$ B-Bcl-2-BAX-RIP1) and invasion pattern of GBM cells in brain in response to OVs and bortezomib. GBM is a serious brain cancer with very low survival rate and major cause of death is regrowth of invasive tumor cells in different locations after surgery. In [46], Kim et al explores tumor growth and invasion patterns in GBM patients based on the injection location of bortezomib and OVs. These studies focus mainly on anti-tumor efficacy of NK therapy and invasion pattern of tumor cells in the presence of bortezomib and OVs through constant treatment protocols. These approaches present challenges in translating the findings into practical clinical applications. In particular, in order to better understand the OV-mediated cell death program and provide personalized care for each cancer patient, it is necessary to develop optimally controlled injection strategies. Due to the safety issues, injection amount of OVs is usually limited and high doses of bortezomib can cause serious side effects. For example, local or IV-administration of OVs can cause adverse reactions such as influenza-like symptoms (vomiting, myalgia, headache, fatigue, elevated body temperature, nausea) and local reactions (pain, rash, erythema, peripheral edema) [83, 84]. Despite the high degrees of anti-tumor effects, bortezomib can also induce serious side effects such as nausea, diarrhea, tiredness, low platelets, fever, and low white blood cell count [85–87]. On the other hand, low level of OVs and bortezomib decreases the overall anti-tumor efficacy due to virus clearance and blood-brain barrier (BBB). Therefore, appropriate level of OVs and bortezomib need to be controlled for injection into patient's body in order to avoid serious side effects and to obtain maximal clinical outcomes. In our framework based on the detailed hybrid type of mathematical model, we used an optimal control theory in order to maximize the anti-tumor efficacy and minimize the side effects and costs associated with administration at clinics by controlling the intracellular cell death program. We also investigated the dynamical systems of intracellular module in terms of apoptosis, oncolysis, and necroptosis in much more detail. This analysis provides a platform of developing more efficient next generation of OVs and another drugs targeting the necroptosis signaling pathway. Hence, we aim to obtain optimal treatment regimens (including timing and dosages) for OV and bortezomib, striking a balance where cancer cell eradication is maximized, while concurrently minimizing undesirable side effects and financial expenditures. The OV/bortezomib-mediated intracellular signaling pathways of apoptosis, necroptosis, and oncoly-



sis in cell death programs are very complex biological system itself, providing fundamentally different mechanism of eradicating tumor cells. The necroptosis pathway plays a key role in cancer therapy including OV therapy. For example, anti-cancer drugs such as doxorubicin can increase oncolytic effect significantly ( $> 100$ -fold in breast cancer) by enhancing OV replication and inducing apoptosis and necroptosis [88]. Other research groups found that a radiation therapy can induce necroptosis in cancer progression [89]. However, it is poorly understood how these cell death programs work in OV therapy in detail. Thus, better understanding of this complex cell-death program itself can shed light into developing a new, more effective anti-cancer drug targeting NF $\kappa$ B-Bcl2-BAX-RIP1 in an OV combination therapy by manipulating the signaling network. Our findings enable the proposal of sophisticated optimal treatment strategies in terms of controlling the precise components at the gene level within a tumor cell rather than a population level (cf. [47]). Furthermore, detailed mathematical analysis of the intracellular cell death cascade and optimally controlled injection schedule can provide a general framework for the pharmaceutical companies to find new compounds targeting signaling pathways in OV therapy. We employed an optimal control formulation to strategically reduce tumor size by triggering both necroptosis and apoptosis through modulating intracellular signaling pathways (NF $\kappa$ B/Bcl2, BAX, RIP1), while managing the cumulative administration costs of bortezomib and OVs. Our results provide efficient and cost-effective therapeutic management schemes for OVs and bortezomib, taking into account overall anti-tumor efficacy.

## 2. Materials and methods

### 2.1. Mathematical model

In this work, we investigate the complex interactions between tumor cells and other therapeutic agents such as bortezomib ( $B$ ) and oncolytic virus ( $v$ ) incorporating an intracellular pathway using a mathematical model. Tumor cells are classified as : Uninfected ( $x$ ), infected ( $y$ ), and necrotic tumor ( $n$ ) cells. Four intracellular components involved in the cell-death program are considered: I $\kappa$ B ( $S$ ), NF $\kappa$ B ( $F$ ), BAX ( $A$ ), and RIP1 ( $R$ ). The regulatory network in Figure 2 describes the complex interactions among the cellular components and intracellular modules. In the model, we consider a tumor microenvironment where (i) initially uninfected tumor cells ( $x$ ) grow (i.e., initial condition of  $x$  is always positive.) (ii) uninfected tumor cells ( $x$ ) become infected tumor cells ( $y$ ) under intracellular oncolysis condition in response OV treatment (iii) bortezomib alone can kill tumor cells under intracellular apoptosis condition (iv) uninfected tumor cells ( $x$ ) become infected tumor cells ( $y$ ) under intracellular necroptosis condition in response both OV treatment and bortezomib, leading to necroptotic death.

Following administration, OVs navigate toward the tumor site and infiltrate the target cancer cells. Within these cells, OVs vigorously replicate generating a substantial viral population. As the infected cancer cells disintegrate, OVs are released, instigating the infection-elimination process anew.

Bortezomib alone, can induce cancer cell death through a typical programmed cell-death pathways, involving apoptotic signaling cascade. Conversely, the combined therapy of bortezomib and OV orchestrates a synergistic assault on cancer cells, harnessing necroptotic signaling pathways to achieve a heightened level of cell destruction.

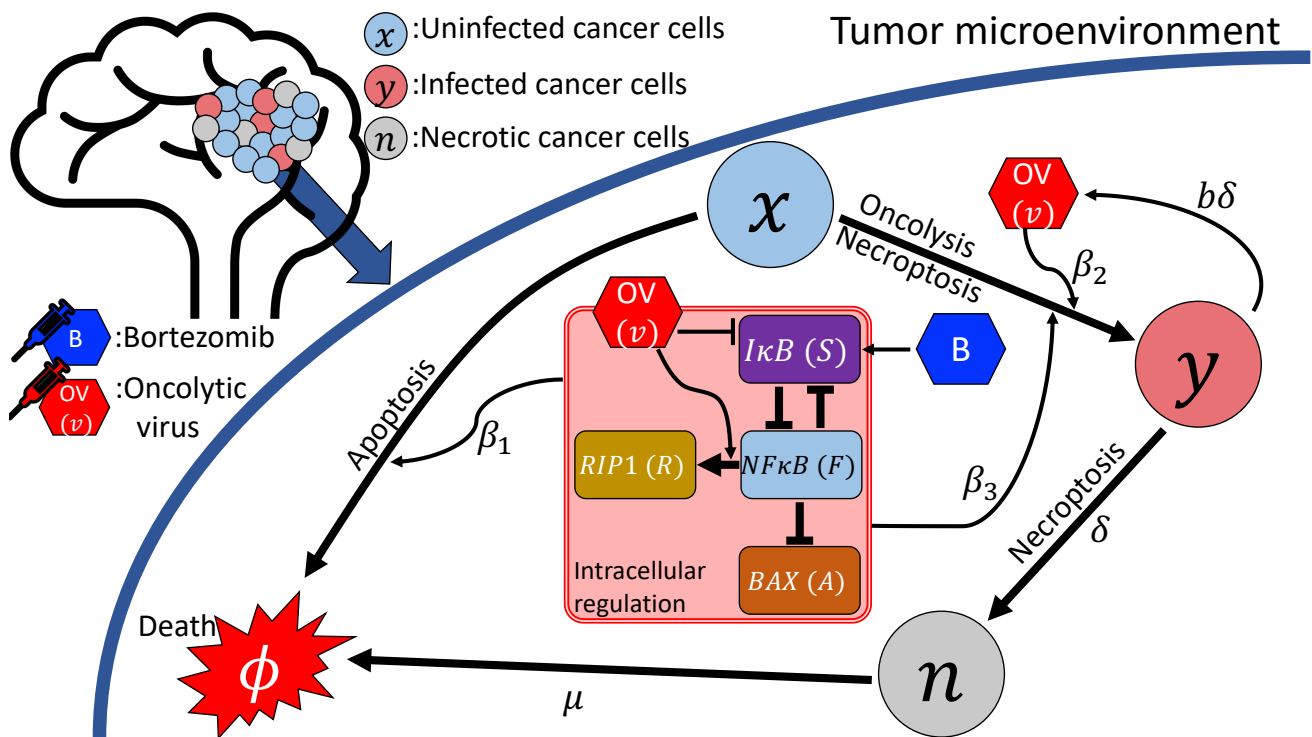


**Figure 2.** A regulatory network in the tumor microenvironment influenced by therapeutic agents, bortezomib and OV. These agents disrupt the intracellular signaling pathways (I $\kappa$ B , NF $\kappa$ B , BAX, RIP1) that could lead to cell death, apoptosis or necroptosis.

The network of the model is shown in Figure 2 and the corresponding model dynamics can be described by a system of ordinary differential equations in a dimensionless form as follows:

$$\frac{dS}{dt} = \lambda_B \frac{B}{1 + \alpha \frac{v}{k+v}} + \sigma_1 \frac{\sigma_9^2}{\sigma_9^2 + \sigma_4 F^2} - S, \quad (2.1)$$

$$\frac{dF}{dt} = \sigma_7 + \sigma_2 \frac{\sigma_{10}^2}{\sigma_{10}^2 + \sigma_5 S^2} - \omega_1(D)F, \quad (2.2)$$

$$\frac{dA}{dt} = \sigma_8 + \sigma_3 \frac{\sigma_{11}^2}{\sigma_{11}^2 + \sigma_6 F^2} - \omega_2 A, \quad (2.3)$$

$$\frac{dR}{dt} = \sigma_{12} + \sigma_{13}[oHSV]F - \omega_3 R, \quad (2.4)$$

$$\frac{dx}{dt} = \lambda x \left(1 - \frac{x}{x_0}\right) - \beta_1 x B I_{apop} - \beta_2 x v I_{oncol} - \beta_3 x v I_{necrop}, \quad (2.5)$$

$$\frac{dy}{dt} = -\delta y + \beta_2 x v I_{oncol} + \beta_3 x v I_{necrop}, \quad (2.6)$$

$$\frac{dn}{dt} = \delta y - \mu n, \quad (2.7)$$

$$\frac{dv}{dt} = u_v + b\delta y(1 + \alpha_1 B) - \gamma v, \quad (2.8)$$

$$\frac{dB}{dt} = u_B - (\mu_1 x + \mu_2 y) \frac{B}{k_B + B} - \mu_B B. \quad (2.9)$$

Here,  $\lambda_B$  is the signaling activation rate of I $\kappa$ B in response to bortezomib signal  $B$ , which is inhibited by the presence of OVs. So,  $[oHSV]$  indicates a response switch function of OVs ( $v$ ) in the form,  $[oHSV] = \frac{v}{k+v}$  with a Hill-type parameter  $k$ . This I $\kappa$ B activity is inhibited by NF $\kappa$ B ( $F$ ) with inhibition strength  $\sigma_4$ , autocatalytic enhancement parameter  $\sigma_1$ , and Hill-type parameters  $\sigma_9$ . In a similar fashion, the inhibition processes of NF $\kappa$ B ( $F$ ) and BAX ( $A$ ) by I $\kappa$ B and NF $\kappa$ B, are represented by corresponding parameters  $\sigma_5, \sigma_2, \sigma_{10}$  and  $\sigma_6, \sigma_3, \sigma_{11}$ , respectively. Here,  $\omega_1(t)$  may depend on drugs that enhance NF $\kappa$ B degradation, i.e.,  $\omega_1(D) = \omega_1^\dagger e^D$  where  $D$  is a concentration of a NF $\kappa$ B inhibitor. Here, the drug concentration  $D$  is a constant. The signaling sources and decay rates of NF $\kappa$ B, BAX, and RIP1 are represented by  $\sigma_7, \sigma_8, \sigma_{12}$  and  $\omega_1, \omega_2$ , and  $\omega_3$ , respectively. The third term on the right hand side of Eq (2.1) indicates the dimensionless natural decay of I $\kappa$ B. The same response switch function  $[oHSV]$  in Eq (2.4) is used for activation of RIP1 in the presence of OVs in the system. Population dynamics of uninfected tumor cells in Eq (2.5) consists of logistic growth with the growth rate  $\lambda$  and carrying capacity  $x_0$ , bortezomib-induced cell killing with the apoptotic death rate  $\beta_1$ , infection process with infection rate  $\beta_2$ , and massive tumor cell killing with necroptotic death rate  $\beta_3$ . An uninfected tumor cell is infected when an oncolytic virus (OV) or a group of OVs enter this tumor cell and replicate upto 10,000-fold, initiating cell death program (either oncolysis and necroptosis) in response to OV therapy. Therefore, the indicator functions  $I_{oncol}$  and  $I_{necrop}$  reflect this infection process and the transition  $x \rightarrow y$ . After infection and confirmation of the cell fate (either oncolysis or necroptosis), the infected tumor cells go through the subsequent, cell death process which is reflected in the  $y \rightarrow n$  transition in the model. Here,  $I_{apop}, I_{oncol}, I_{necrop}$  are indicator functions for apoptotic, oncolytic, and necroptotic status, respectively, based on up- or down-regulation of NF $\kappa$ B, BAX, and RIP1:

$$I_{apop} = \begin{cases} 1 & \text{if apoptosis} \\ 0 & \text{otherwise} \end{cases}, \quad I_{oncol} = \begin{cases} 1 & \text{if oncolysis} \\ 0 & \text{otherwise} \end{cases}, \quad I_{necrop} = \begin{cases} 1 & \text{if necroptosis} \\ 0 & \text{otherwise} \end{cases}. \quad (2.10)$$

The exact definition of these status will be defined in the next section. Infected tumor cells ( $y$ ) from the uninfected tumor population are cleared to dying tumor population ( $n$ ) at a death rate  $\delta$  and these necrotic population are cleared from the population system at a death rate  $\mu$ . OVs are supplied at a rate  $u_V$  and are able to replicate from lysis of infected cancer cells at a rate  $b\delta y$  with doubling number  $b$  in the absence of bortezomib ( $B$ ). Injection of bortezomib in addition to OV therapy enhances viral replication at additional rate  $\alpha_1 B$ , inducing synergistic anti-cancer effect. OVs are cleared from the system at a rate  $\gamma$ . Bortezomib is injected at a rate  $\mu_B$ , internalized in uninfected and infected cancer cells at degradation rates  $\mu_1$  and  $\mu_2$ , respectively, and cleared from the system at a decay rate  $\mu_B$ .

A dimensional version of equations corresponding to Eqs (2.1)–(2.9) and the nondimensionalization provided in the Supplementary material (Supporting information S1 File). Matlab (Mathworks) software is used to simulate the transient dynamics of the model and to obtain the numerical results for the optimal control problems. Table 1 provides the full list of parameters, its meaning and corresponding values used in the model.

**Table 1.** Parameters of the non-dimensionalized in the model.

Par	Description	Values	Ref
Intracellular dynamics			
$\lambda_B$	Bortezomib signaling scaling factor	1.9	[46]
$\alpha$	Inhibition strength of bortezomib by oHSV	30	[46]
$\sigma_1$	Autocatalytic enhancement rate of I $\kappa$ B	4	[46]
$\sigma_9$	Hill-type parameter	1.0	[46]
$\sigma_4$	Inhibition strength of I $\kappa$ B by the NF $\kappa$ B-Bcl-2 complex	2.2	[46]
$\sigma_7$	Signaling strength of the NF $\kappa$ B-Bcl-2 complex	0.07	[46]
$\sigma_2$	Autocatalytic enhancement rate of the NF $\kappa$ B-Bcl-2 complex	1.33	[46]
$\sigma_{10}$	Hill-type parameter	1.0	[46]
$\sigma_5$	Inhibition strength of the NF $\kappa$ B-Bcl-2 complex by I $\kappa$ B	1	[46]
$\omega_1$	Decay rate of NF $\kappa$ B-Bcl-2 complex	0.3	[107, 108]
$\sigma_8$	Signaling strength of BAX	0.0033	[46]
$\sigma_3$	Autocatalytic enhancement rate of BAX	0.111	[46]
$\sigma_{11}$	Hill-type parameter	1.0	[46]
$\sigma_6$	Inhibition strength of BAX by the NF $\kappa$ B-Bcl-2 complex	1	[46]
$\omega_2$	Decay rate of BAX	0.02	[107–109]
$\sigma_{12}$	Signaling strength of RIP1	0.1	[46]
$\sigma_{13}$	Activation rate of RIP1 in the presence of OV $s$	0.13	[46]
$\omega_3$	Decay rate of RIP1	0.139	[107, 108, 110]
$k$	Hill type parameter of oHSV switching	0.01 $v^*$	[46]
Cancer cells			
$\lambda$	proliferation rate of tumor cells	$4 \times 10^{-3}$	[46, 57]
$x_0$	Carrying capacity of uninfected tumor cells	1	[38, 45, 46, 57]
$\beta_1$	Bortezomib-induced apoptosis rate of tumor cells	$2 \times 10^{-4}$	[46]
$\beta_2$	Oncolysis rate of tumor cells	$3 \times 10^{-4}$	[45, 46, 57]
$\beta_3$	Necroptosis rate of tumor cells	$5 \times 10^{-4}$	[46]
$\delta$	infected cell lysis rate	$4.4 \times 10^{-3}$	[45, 57]
$\mu$	Removal rate of dead cells	$2.3 \times 10^{-3}$	[45, 46, 57]
Anticancer drugs			
$b$	Burst size of infected cells	50	[46, 57]
$\alpha_1$	bortezomib-induced viral replication rate	1	[45, 46]
$\gamma$	clearance rate of viruses	$1.8 \times 10^{-3}$	[45, 57]
$\mu_1$	consumption rate of bortezomib by uninfected tumor cells	0.2075	[45, 46]
$\mu_2$	consumption rate of bortezomib by infected tumor cells	0.2075	[45, 46]
$k_B$	Hill-type parameter	1	[45, 46]
$\mu_B$	decay rate of bortezomib	0.03	[46, 111, 112]
Reference values of main variables			
$S^*$	Concentration of I $\kappa$ B	0.05 $\mu$ M	[113, 114]
$F^*$	Concentration of the NF $\kappa$ B-Bcl2 complex	0.5 $\mu$ M	[113–116]
$A^*$	Concentration of BAX	0.1 $\mu$ M	[117]
$R^*$	Concentration of RIP1	5.0 $\mu$ M	[118]
$x^*$	Uninfected cell density	$10^6$ cells/mm $^3$	[45, 57, 119]
$y^*$	Infected cell density	= $x^*$	[45, 57, 119]
$n^*$	Dead cell density	= $x^*$	[45, 57, 119]
$v^*$	Virus concentration	$2.2 \times 10^8$ virus/mm $^3$	[45, 57, 119]
$B^*$	Bortezomib concentration	$1.0 \times 10^{-11}$ g/mm $^3$	[6, 43, 45]

## 2.2. Optimal control problem

The optimal control theory was used to yield an optimal administration strategies of OV $s$  and bortezomib that minimizes tumor cell populations (uninfected and infected tumor cells) and associated costs. Our goal is to obtain feasible therapeutic schedule of  $u_V$  and  $u_B$  to reduce the tumor size with minimal administrative costs. The controls  $u_V$  and  $u_B$  represent dosages of OV $s$  and bortezomib, respectively.

These controls are assumed to be bounded. That is, the control sets are defined as

$$u_V(t) \in [0, u_V^{max}] \text{ and } u_B(t) \in [0, u_B^{max}] \text{ for all } t \in [t_s, t_f], \quad (2.11)$$

where  $u_V^{max}$  and  $u_B^{max}$  are the maximum dosage of OV and bortezomib, respectively, which could be administered in a given treatment period  $[t_s, t_f]$  (where  $t_s$  is the start time of treatment with optimal control applied, and  $t_f$  is the end time).

Two distinct cost functionals are formulated to facilitate alternating administrations of OVs and bortezomib, enhancing their synergistic efficacy against cancer cells. In the first formulation, both integrands involve linear combination of uninfected  $x(t)$ , infected  $y(t)$  and quadratic control. This quadratic form guarantees a strictly convex Hamiltonian and a unique minimizer, rendering the mathematical problem more tractable. Incorporating quadratic controls within the cost function effectively simulates the detrimental repercussions of excessive drug administration, a strategy observed in multiple studies [32, 82, 90–93]. However, the use of such quadratic functionals lacks robust biological justification, raising concerns about the validity of its simplifying assumptions [94]. The quadratic functional types may not be commonly motivated by biological systems making its simplifying model assumptions bit questionable and ambiguous [94]. However, its use also showed qualitatively significant outcomes in terms of incorporating the intrinsic nonlinearity of the given problem [90, 95]. Thus, the quadratic controls in the cost function has been used in controlling the adverse effects of use of too much therapeutic drugs in various works [32, 82, 90–93]. In cancer immunotherapy, a type of isoperimetric optimal controls has been applied [79–81]. This leads to the formulation of an alternative cost functional, where linear controls are involved, supplemented by a penalty function serving as a guide for controlled implemented.

- 1) **Quadratic controls** This strategy proposes a sequential administration of OV and bortezomib, minimizing both their dosages and the levels of uninfected ( $x(t)$ ) and infected cancer cells ( $y(t)$ ). Employing quadratic controls lead to the following cost functional

$$J(u_V(t), u_B(t)) = \int_{t_s}^{t_f} \left( x(t) + y(t) + C_1 \frac{u_V^2(t)}{2} \right) dt + \int_{t'_s}^{t'_f} \left( x(t) + y(t) + C_2 \frac{u_B^2(t)}{2} \right) dt. \quad (2.12)$$

- 2) **Linear controls with constraint** In this approach, linear controls are employed to emulate a biologically plausible regulatory mechanism. To achieve the desired effect of inducing necroptosis, a sigmoid function is integrated that ensures a sustained and optimal concentration of bortezomib. The cost functional yields

$$J(u_V(t), u_B(t)) = \int_{t_s}^{t_f} \left( x(t) + y(t) + C_3 u_V(t) \right) dt + \int_{t'_s}^{t'_f} \left( C_4 u_B(t) + \frac{B_5}{1 + e^{p(B - t_{hB})}} \right) dt. \quad (2.13)$$

Our goal is to find optimal administration of both OV and bortezomib ( $u_V^*(t)$  and  $u_B^*(t)$ ), identifying optimal dosages under the framework of optimal control theory. The principle technique for such an optimal control problem is to solve a set of “*necessary condition*” that an optimal control and corresponding state must satisfy. The necessary conditions we derived were developed by Pontryagin. He introduced the concept of ‘adjoint functions’ to incorporate differential equations into the objective function. Adjoint functions serve a similar purpose to the Lagrange multiplier of multivariate calculus,

which adds constraints to functions of several variables that are being maximized or minimized [62,96]. We perform numerical simulations by employing a fourth-order iterative Runge-Kutta method. Commencing with the initial conditions and an initial control estimate, we solve the state equations using the forward scheme. Furthermore, the adjoint equations are solved using the backward scheme, ensuring compliance with the transversality conditions. Control updates involve a convex combination of the previous controls and values derived from the characterizations. This methodology, recognized as the Forward-Backward Sweep Method (FBSM), has demonstrated convergence [94]. See supporting information S1 File for more details.

### 3. Results

#### 3.1. Intracellular dynamics

The fundamental structure of four phenotypic modes in response to various bortezomib levels in the absence and presence of OVs are represented in Figure 3. Specifically, Figure 3(A),(B) illustrate the steady states of three key intracellular variables: NF $\kappa$ B (represented by blue solid curve), BAX (depicted by the dashed red curve), and RIP1 (shown as the dotted yellow curve). These plots delineate the behavior of these variables under varying bortezomib ( $B$ ) concentrations, when OVs are absent ( $v = 0$  in Figure 3(A)) and present ( $v = 1$  in Figure 3(B)).

In the absence of OV within the system, we observe elevated levels of NF $\kappa$ B, coupled with low levels of both BAX and RIP1 in response to lower levels of bortezomib. This dynamic pattern prevents the initiation of bortezomib-induced apoptosis, as the key apoptotic gene, BAX, remains suppressed. As the bortezomib concentration increases, a shift occurs: NF $\kappa$ B is down-regulated, while RIP1 maintains a low level; moreover, the BAX level transitions to an overexpression state, triggering programmed cell death, specifically apoptosis (Figure 3(A)). However, the intracellular dynamics of NF $\kappa$ B, BAX, and RIP1 undergo a significant transformation in the presence of OV when responding to bortezomib stimuli. Both NF $\kappa$ B and RIP1 consistently sustain high levels irrespective of bortezomib concentrations, while the BAX level remains consistently low (Figure 3(B)). This particular state signifies the activation of necroptotic signaling (depicted within the pink box in Figure 3(B)) under conditions of elevated bortezomib levels. Conversely, when bortezomib stimulus is limited, cell demise ensues through oncolysis (illustrated by the green box in Figure 3(B)), rather than necroptosis.

By defining thresholds for these intracellular variables,  $th_F = 1.7$  for NF $\kappa$ B,  $th_A = 1.7$  for BAX,  $th_R = 1.7$  for RIP1, and  $th_B = 0.1$  for bortezomib, we can delineate four different phenotypic modes, namely the anti-apoptotic ( $\mathbb{T}_t$ ), apoptotic ( $\mathbb{T}_a$ ), necroptotic ( $\mathbb{T}_n$ ), and oncolysis ( $\mathbb{T}_o$ ) phases as follows:

$$\mathbb{T}_t = \{(F, A, R) \in \mathbb{R}^3 : F > th_F, A < th_A, R < th_R\}, \quad (3.1)$$

$$\mathbb{T}_a = \{(F, A, R) \in \mathbb{R}^3 : F < th_F, A > th_A, R < th_R\}, \quad (3.2)$$

$$\mathbb{T}_n = \{(F, A, R, B) \in \mathbb{R}^4 : F > th_F, A < th_A, R > th_R, B > th_B\}, \quad (3.3)$$

$$\mathbb{T}_o = \{(F, A, R, B) \in \mathbb{R}^4 : F > th_F, A < th_A, R > th_R, B < th_B\}. \quad (3.4)$$

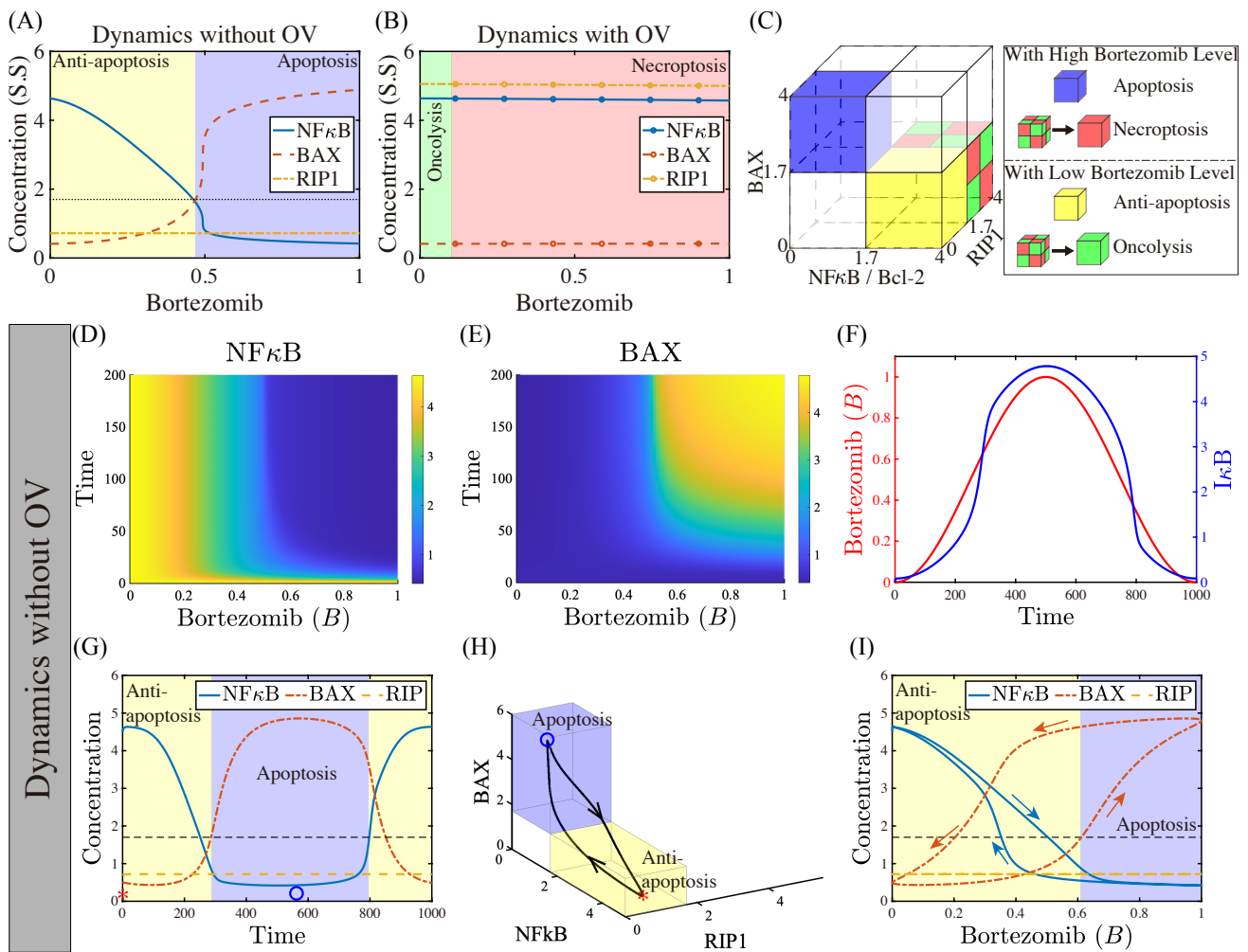


**Figure 3.** Bifurcation diagram of intracellular variables and characterization of the cell death program. (A,B) Steady states (stable) of intracellular variables (NF $\kappa$ B, BAX, and RIP1) in response to high and low bortezomib stimuli in the absence ((A),  $v = 0$ ) and presence ((B),  $v = 1$ ) of OV in the system. (C) Characterization of four different modes based on expression levels of NF $\kappa$ B/Bcl-2, BAX, and RIP1: Apoptosis, Anti-apoptosis, Necroptosis, and Oncolysis. (D,E) Time courses of concentrations of NF $\kappa$ B (D) and BAX (E) for various bortezomib levels ( $0 \leq B \leq 1$ ). (F) Time course of the I $\kappa$ B level in response to a time-dependent bortezomib input ( $B(t) = -0.5 \cos(\frac{\pi}{500}t + 0.5)$ ). (G–I) Concentrations (G) of key intracellular variables (NF $\kappa$ B, BAX, and RIP1) and corresponding trajectories in the  $F$ – $R$ – $A$  plane (H) and bifurcation diagram (I) in response to a fluctuating bortezomib stimulus and I $\kappa$ B in (F). Initial conditions used in the simulations:  $S(0) = 0$ ,  $F(0) = 4.5$ ,  $A(0) = 0.5$ ,  $R(0) = 0.7$ .  $D = 0$ .

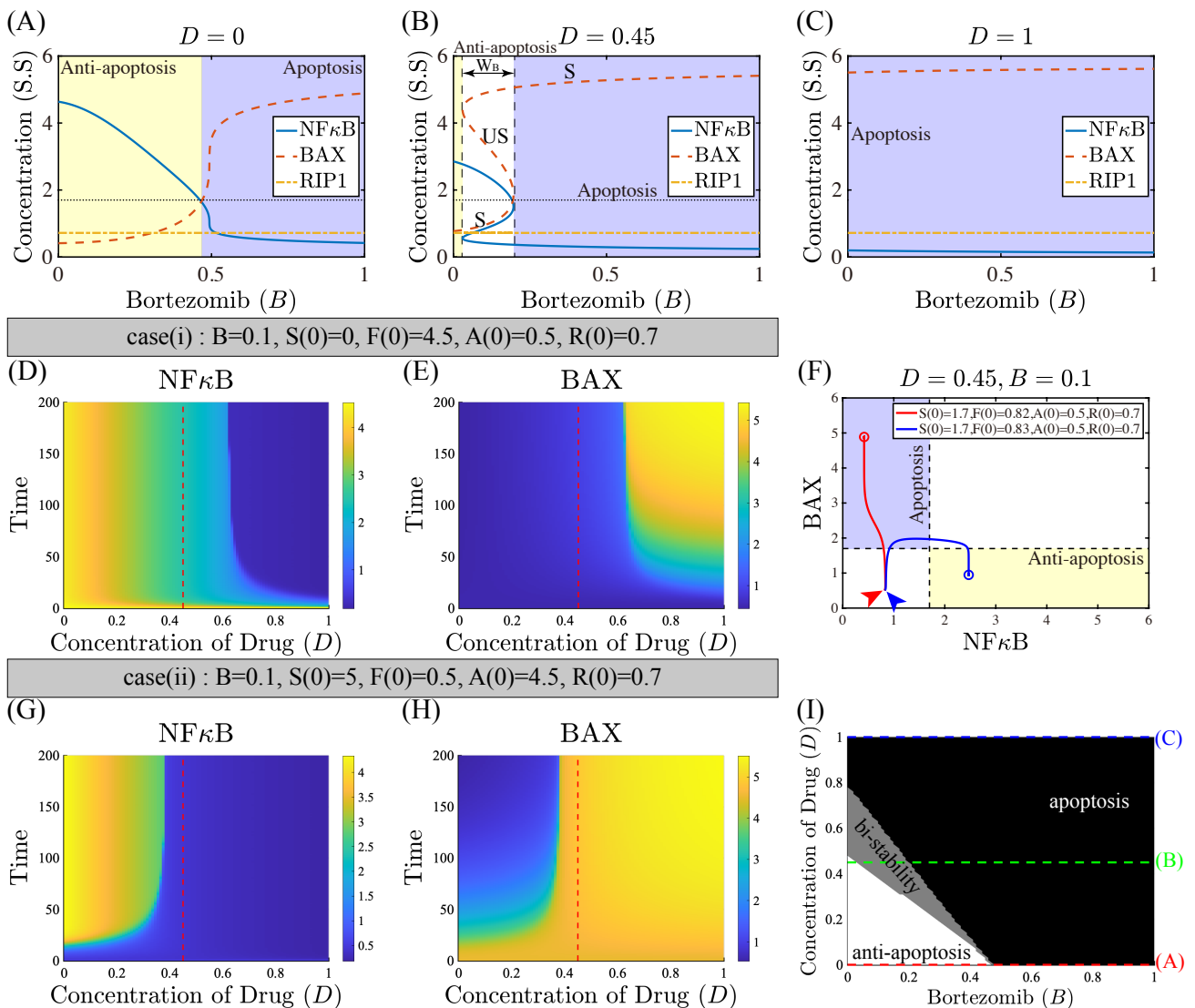


**Figure 4.** Effect of anti-NFκB antibodies on dynamics of apoptotic death in cancer (A–C) Steady states of intracellular variables (NFκB, BAX, and RIP1) for various bortezomib stimuli in the absence ((A),  $D = 0$ ) and presence ( $D = 0.45$  in (B) and  $D = 1$  in (C)) of anti-NFκB drug in the system. In Figure 4A,4C, the equilibrium is stable. In Figure 4B the upper and lower branches are stable while the middle one is unstable (US). (D,E) Time courses of concentrations of NFκB (D) and BAX (E) in response to various drug levels ( $0 \leq D \leq 1$ ) when  $B = 0.1$  with initial conditions:  $S(0) = 0, F(0) = 4.5, A(0) = 0.5, R(0) = 0.7$ . (F) Trajectories of solutions in the  $F - A$  plane when  $D = 0.45, B = 0.1$  with initial conditions:  $S(0) = 1.7, F(0) = 0.82, A(0) = 0.5, R(0) = 0.7$  for red curve, and  $S(0) = 1.7, F(0) = 0.83, A(0) = 0.5, R(0) = 0.7$  for the blue curve. (G,H) Time courses of concentrations of NFκB (G) and BAX (H) in response to various drug levels ( $0 \leq D \leq 1$ ) when  $B = 0.1$ . Initial condition  $S(0) = 5, F(0) = 0.5, A(0) = 4.5, R(0) = 0.7$ . (I) Characterization of apoptosis, bistability, anti-apoptosis regions in the  $B - D$  plane.

Figure 3(C) illustrates the anti-apoptosis (yellow cube), apoptosis (blue cube), necroptosis (red



cube), and oncolysis (green cube) modules in a NF $\kappa$ B-BAX-RIP1 state space. Figure 3(D),(E) show temporal dynamics of concentrations of NF $\kappa$ B and BAX, respectively, with various fixed bortezomib levels ( $0 \leq B \leq 1$ ), illustrating convergent behaviors of two key intracellular variables. Sharp contrast in expression levels at final time ( $t = 200$ ) in both NF $\kappa$ B and BAX reflects different modes: anti-apoptosis (yellow cube in Figure 3(C)) for low bortezomib levels ( $0 \leq B \leq 0.46$ ) and apoptosis (blue cube in Figure 3(C)) phases for high bortezomib levels ( $0.46 \leq B \leq 1$ ). In Figure 3(F)–(I), we investigate the temporal dynamics of the intracellular module in response to a fluctuating bortezomib stimulus ( $B(t) = -0.5 \cos(\frac{\pi}{500}t + 0.5)$ ). The concentration of I $\kappa$ B undergoes a sudden increase surpassing that of  $B(t)$ , and reaches its peak coinciding with that of bortezomib's maximum concentration. Conversely, as  $B(t)$  decreases, the concentration of I $\kappa$ B takes a downward course, undergoing an abrupt reduction that surpasses the decline in bortezomib levels. This sequence culminates a cycle of bortezomib-triggered activation and deactivation. The inherent mutual inhibition between I $\kappa$ B and NF $\kappa$ B, as described in Eqs (2.1) and (2.2), gives rise to a pivotal dynamic. Specifically, the upward shift (from down-regulation to up-regulation) of I $\kappa$ B during the initial stimulus phase ( $0 \leq t \leq 500$ ) induces a downward transition (from up-regulation to down-regulation) in NF $\kappa$ B and brings about an upward transition (from down-regulation to up-regulation) in BAX. This orchestrated sequence results in a significant phenotypic switch, steering the system from an anti-apoptosis state to an apoptosis mode (as depicted in Figure 3(G)).

Bortezomib has been demonstrated to induce cancer cell elimination through diverse mechanisms, including the suppression of the NF $\kappa$ B pathway. Furthermore, it effectively inhibits the NF $\kappa$ B-mediated tumor growth enhancement by suppressing the degradation of I $\kappa$ B, thereby manifesting its multifaceted antitumor effects [97–101]. Thus, bortezomib can successfully induce apoptotic death of cancer cells in the absence of OV as illustrated in Figure 3(F)–(H) and corroborated by experimental evidences [97–101]. As the value of  $B(t)$  is reduced during the second half of the period ( $500 \leq t \leq 1000$ ), the backward switch (NF $\kappa$ B (low $\rightarrow$ high); BAX (high $\rightarrow$ low)) follows, leading to the reverse ( $\mathbb{T}_a \rightarrow \mathbb{T}_t$ ) transition (Figure 3(G)). This loop of forward and backward transitions with initial (red asterisk) and mid point (blue circle) on the trajectory curve is shown in Figure 3(H). This illustrates the dynamic movement of concentrations of key intracellular molecules in the bifurcation diagram, forming a loop of that characterizes a cell death program ( $\mathbb{T}_t \rightarrow \mathbb{T}_a \rightarrow \mathbb{T}_t$ , Figure 3(H)), in response to a fluctuating bortezomib stimulus (Figure 3(I)).

In Figure 4, we investigate the effect of anti-NF $\kappa$ B antibodies on the dynamic progression of apoptotic cell death within cancer cells. These antibodies serve as valuable tools to study the activation and regulation of NF $\kappa$ B signaling pathways in various biological contexts, including cancer, inflammation, and immune responses. In therapeutic applications, targeting NF $\kappa$ B with specific antibodies may have potential applications in treating diseases characterized by aberrant NF $\kappa$ B activity, such as certain autoimmune disorders and cancers [102, 103]. Figure 4(A)–(C) depict the steady states of intracellular variables (NF $\kappa$ B, BAX, and RIP1) for various bortezomib stimuli in the absence (Figure 4(A),  $D = 0$ ) and presence ( $D = 0.45$  in Figure 4(B) and  $D = 1$  in Figure 4(C)) of anti-NF $\kappa$ B drug in the system. The results demonstrate that the area of apoptosis expands as the dose of NF $\kappa$ B antibody increase from 0 to 1. This suggests that apoptosis can be induced even with a small amount of bortezomib, and its effect becomes more prominent as the dose of NF $\kappa$ B antibody increases. Figure 4(D),(E) show the time courses of concentrations of NF $\kappa$ B (Figure 4(D)) and BAX (Figure 4(E)) in response to various drug levels ( $0 \leq D \leq 1$ ) when  $B = 0.1$  with nitial condition

$S(0) = 0, F(0) = 4.5, A(0) = 0.5, R(0) = 0.7$ . Figure 4(G),(H) illustrate the time courses of concentrations of NF $\kappa$ B (Figure 4(G)) and BAX (Figure 4(H)) in response to various drug levels ( $0 \leq D \leq 1$ ) when  $B = 0.1$  with initial condition  $S(0) = 5, F(0) = 0.5, A(0) = 4.5, R(0) = 0.7$ . Figure 4(F) depicts the trajectories of solutions in the  $F - A$  plane when  $D = 0.45, B = 0.1$ . Initial conditions used for the red curve are  $S(0) = 1.7, F(0) = 0.82, A(0) = 0.5, R(0) = 0.7$  while for the blue curve are  $S(0) = 1.7, F(0) = 0.83, A(0) = 0.5, R(0) = 0.7$ . The bistability region exist when the level of NF $\kappa$ B antibody is intermediate. Indeed, near the bistable point, small changes in the initial values can lead to convergence in opposite directions, resulting to different treatment outcomes. Therefore, when proposing a treatment strategy in the early stages, it is crucial to carefully consider the condition of intracellular signaling. The sensitivity to initial conditions near the bistable point highlights the need for precision and thorough analysis when designing therapeutic interventions to achieve the desired treatment outcomes. Figure 4(I) shows the characterization of apoptosis, bistability, anti-apoptosis regions in the  $B - D$  plane.

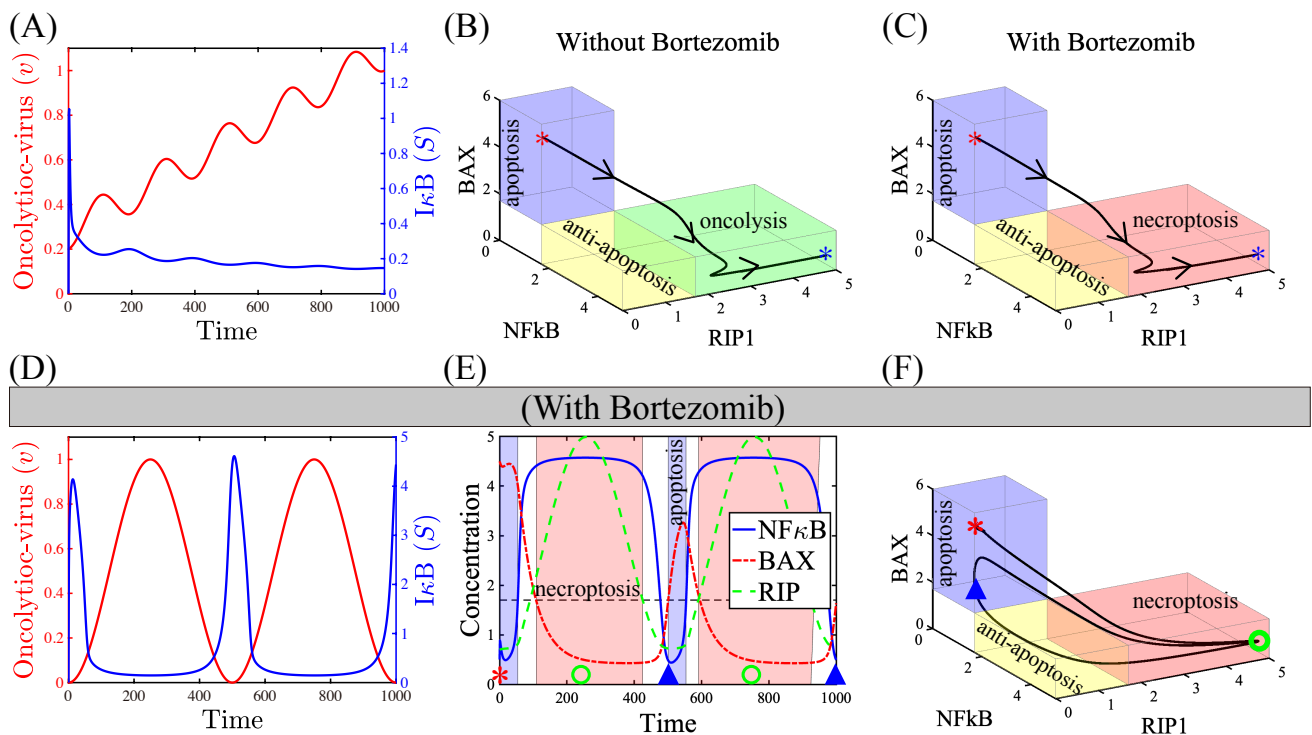


**Figure 5.** The effect of Bortezomib on determining the phenotypic states in OV therapy. (A–C) Trajectories of solutions of intracellular variables (NF $\kappa$ B, BAX, and RIP1) in the  $F - A - R$  space in the absence (B) and presence (C) of bortezomib in response to OV stimuli (A):  $v(t) = -\frac{2}{25} \cos \frac{\pi}{100}t + 0.0008t + 0.28$ . (D–F) Time courses (D) and trajectories (E) of solutions of intracellular variables (NF $\kappa$ B, BAX, and RIP1) in the  $F - A - R$  space in the presence of bortezomib in response to fluctuating OV stimuli (A):  $v(t) = -\frac{1}{2} \cos \frac{\pi}{250}t + 0.5$ . Initial conditions:  $S(0) = 0, F(0) = 0.5, A(0) = 4.5, R(0) = 0.7, v(0) = 0.2$ . Bortezomib level:  $B = 0$  (in (B)), 1 (in (C)).

Within oncolytic virotherapy (OV therapy), the mere presence of active OV's proves adept at eradicating cancer cells through oncolysis, that avoids the initiation of necroptosis signaling pathways,

even in the absence of bortezomib. Intriguingly, empirical evidence has illuminated the amalgamation of therapies, wherein OV<sub>s</sub> and bortezomib are combined, induces a synergistic impact, notably enhancing the efficacy of cancer cell eradication [6, 43]. We investigate the temporal dynamics of intracellular variables in Eqs (2.1)–(2.4) in response to fluctuating OV supply in the absence and presence of bortezomib. In response to increasing OV input described by  $v(t) = -\frac{2}{25} \cos \frac{\pi}{100}t + 0.0008t + 0.28$  (Figure 5(A)), the system starting from the same apoptotic status (red asterisks in Figure 5(B),(C)) converges to oncolytic phenotype (blue asterisk in Figure 5(B)) and necroptotic mode (blue asterisk in Figure 5(C)) in the absence ( $B = 0$ ) and presence ( $B = 1$ ) of bortezomib, respectively. In other words, the typical apoptotic cell death program in response to bortezomib transits to more severe cell death program, i.e., necroptosis (red asterisk  $\rightarrow$  blue asterisk in Figure 5(C)), when oncolytic virus is present in the tumor microenvironment. The phenotypic transition between apoptosis and necroptosis is bidirectional. When OV stimulus fluctuates according to  $v(t) = -\frac{1}{2} \cos \frac{\pi}{250}t + 0.5$ , the initial curve in  $v(t)$  leads to the first transition from the apoptotic mode (red asterisk in Figure 5(F)) to the necroptotic mode (green circle in Figure 5(F)) but it is followed by back-transition to the apoptotic mode (blue triangle in Figure 5(F)) in response to the declining OV level. The second wave of OV stimuli also induces a loop of transition series  $\mathbb{T}_a \rightarrow \mathbb{T}_n \rightarrow \mathbb{T}_a$  by the forward and backward movements.

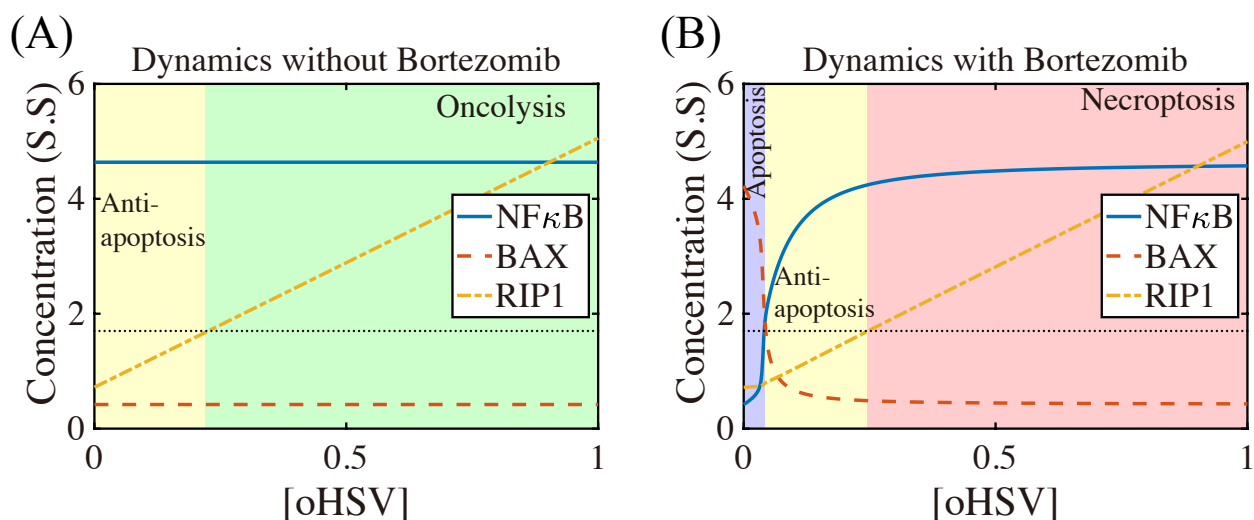


**Figure 6.** Bifurcation diagram of intracellular variables and characterization of the cell death program. (A,B) Steady states of intracellular variables (NF $\kappa$ B, BAX, and RIP1) in response to high and low [oHSV] stimuli in the absence ((A),  $B = 0$ ) and presence ((B),  $B = 1$ ) of bortezomib in the system.

### 3.2. Intracellular dynamics in response to OV<sub>s</sub>

The fundamental structures of four phenotypic modes in response to various bortezomib levels in the absence and presence of OV<sub>s</sub> are represented in Figure 3. Here, we further scrutinized the fundamental structures of four phenotypic modes, discerning their responses to diverse levels of oncolytic viruses in both the absence and presence of bortezomib. Specifically, Figure 6 illustrates the steady states of three key intracellular variables (NF $\kappa$ B, BAX, and RIP1). These plots delineate the behavior of these variables under varying [oHSV] conditions in the absence ( $B = 0$  in Figure 6(A)) and presence ( $B = 1$  in Figure 6(B)) of bortezomib.

NF $\kappa$ B consistently sustains high levels irrespective of [oHSV], while the BAX level remains consistently low (Figure 6(A)). However, the level of RIP1 increases as the [oHSV] increases. This particular state signifies the activation of oncolysis signaling (depicted within the green box in Figure 6(A)) under conditions of elevated [oHSV] levels. Conversely, when [oHSV] stimulation is limited, the cell death program is not initiated, leading to the anti-apoptosis phenotype (illustrated by the yellow box in Figure 6(A)). However, the intracellular dynamics of NF $\kappa$ B, BAX, and RIP1 undergoes a significant transformation in the presence of bortezomib in response to [oHSV] stimuli. In the presence of bortezomib within the system, we observe elevated levels of BAX, coupled with low levels of both NF $\kappa$ B and RIP1 in response to lower levels of [oHSV] (Figure 6(B)). This dynamic pattern prevents the initiation of bortezomib-induced apoptosis, as the key apoptotic gene, BAX, remains suppressed. As the concentration of [oHSV] increases, we have a dramatic shift: NF $\kappa$ B and RIP1 are up-regulated, while the level of BAX remains low, leading anti-apoptosis (yellow box in Figure 6(B)). As the [oHSV] increases further, the RIP1 level transits to an overexpression state, triggering necroptosis (pink box in Figure 6(B)).

### 3.3. Sensitivity analysis

In the main text model, certain parameters lack experimental data and may influence simulation results. We considered all parameters in the intracellular signaling ( $B$ ,  $v$ ,  $\lambda_B$ ,  $\alpha$ ,  $\sigma_1$ ,  $\sigma_9$ ,  $\sigma_4$ ,  $\sigma_7$ ,  $\sigma_2$ ,  $\sigma_{10}$ ,  $\sigma_5$ ,  $\omega_1$ ,  $\sigma_8$ ,  $\sigma_3$ ,  $\sigma_{11}$ ,  $\sigma_6$ ,  $\omega_2$ ,  $\sigma_{12}$ ,  $\sigma_{13}$ ,  $\omega_3$ ) for sensitivity analysis. We examined the sensitivity of intracellular molecules' activities (IkB, NF $\kappa$ B, BAX, and RIP1) at  $t = 0.1, 1, 10, 100$  to these parameters. A range was selected for each parameter, divided into 10,000 intervals of uniform length. For each of the 20 parameters of interest, a partial rank correlation coefficient (PRCC) value was calculated. PRCC values range between -1 and 1, with the sign determining whether an increase in the parameter value will decrease (-) or increase (+) activities of the intracellular dynamics at a given time. The sensitivity analysis, as described below, followed the method outlined in [104]. In Figure 7, The BAX (activities of apoptosis inducer) level is positively correlated to  $\omega_1$ ,  $\sigma_8$ ,  $\sigma_3$ ,  $\sigma_{11}$  but negatively correlated to  $\omega_2$ . In a similar fashion, the RIP1 (activities of necroptosis or oncolysis inducer) activity is positively correlated to  $\sigma_7$ ,  $\sigma_2$ ,  $\sigma_{10}$ ,  $\sigma_{12}$ ,  $\sigma_{13}$  but negatively correlated to  $\omega_1$ ,  $\omega_3$ . These results are summarized in Table 2.

**Table 2.** Model parameters used in sensitivity analysis and PRCC values of intracellular signaling network (IkB ( $S$ ), NF $\kappa$ B ( $F$ ), BAX ( $A$ ), and RIP1 ( $R$ )) at  $t = 0.1, 1, 10, 100$  h for 20 perturbed parameters ( $B$ ,  $v$ ,  $\lambda_B$ ,  $\alpha$ ,  $\sigma_1$ ,  $\sigma_9$ ,  $\sigma_4$ ,  $\sigma_7$ ,  $\sigma_2$ ,  $\sigma_{10}$ ,  $\sigma_5$ ,  $\omega_1$ ,  $\sigma_8$ ,  $\sigma_3$ ,  $\sigma_{11}$ ,  $\sigma_6$ ,  $\omega_2$ ,  $\sigma_{12}$ ,  $\sigma_{13}$ ,  $\omega_3$ ). A range (minimum and maximum) of 20 perturbed parameters and their baseline are given in the upper table. Sample size  $N = 10,000$ .

Parameter	$B$	$v$	$\lambda_B$	$\alpha$	$\sigma_1$	$\sigma_9$
PRCC( $S$ ,0.1 h)	0.28187	-0.03828	0.26953	-0.33367	0.94918	0.50929
PRCC( $F$ ,0.1 h)	-0.02305	0.01961	-0.02248	0.04351	-0.27969	-0.04106
PRCC( $A$ ,0.1 h)	0.00822	0.00416	-0.01449	-0.01347	-0.01005	-0.00355
PRCC( $R$ ,0.1 h)	-0.00527	0.13183	-0.00513	0.02775	-0.06686	-0.01338

*Continued on next page*

Parameter	$B$	$\nu$	$\lambda_B$	$\alpha$	$\sigma_1$	$\sigma_9$
PRCC( $S$ ,1 h)	0.26056	-0.02550	0.25868	-0.29694	0.82422	0.73676
PRCC( $F$ ,1 h)	-0.07284	0.02242	-0.08059	0.09171	-0.48167	-0.32707
PRCC( $A$ ,1 h)	0.02008	0.00165	0.01746	-0.02042	0.11314	0.05378
PRCC( $R$ ,1 h)	-0.03627	0.11745	-0.04266	0.06355	-0.27849	-0.14751
PRCC( $S$ ,10 h)	0.37318	-0.03499	0.35211	-0.35990	0.55805	0.62897
PRCC( $F$ ,10 h)	-0.09981	0.02151	-0.10770	0.12735	-0.32377	-0.35500
PRCC( $A$ ,10 h)	0.04337	0.00249	0.04355	-0.04101	0.16069	0.14905
PRCC( $R$ ,10 h)	-0.06094	0.07032	-0.07396	0.10494	-0.23546	-0.24755
PRCC( $S$ ,100 h)	0.38143	-0.03454	0.36085	-0.36390	0.51007	0.58888
PRCC( $F$ ,100 h)	-0.09180	0.01882	-0.10493	0.12160	-0.27286	-0.30714
PRCC( $A$ ,100 h)	0.04653	-0.00022	0.02574	-0.01787	0.11811	0.10076
PRCC( $R$ ,100 h)	-0.04955	0.05732	-0.06608	0.09572	-0.17990	-0.19896
Minimum	0	0	0.19	3	0.4	0.1
Baseline	0.5	0.01	1.9	30	4	1
Maximum	5	0.1	5.7	60	8	5
Parameter	$\sigma_4$	$\sigma_7$	$\sigma_2$	$\sigma_{10}$	$\sigma_5$	$\omega_1$
PRCC( $S$ ,0.1 h)	-0.17767	-0.06597	-0.24638	-0.03404	-0.00584	0.02214
PRCC( $F$ ,0.1 h)	0.00846	0.63726	0.96485	0.53649	-0.19325	-0.15541
PRCC( $A$ ,0.1 h)	-0.01288	-0.03460	-0.19312	-0.03172	-0.00515	0.00624
PRCC( $R$ ,0.1 h)	0.02074	0.26024	0.79329	0.14504	-0.05250	-0.04657
PRCC( $S$ ,1 h)	-0.40421	-0.20533	-0.50535	-0.30275	0.12012	0.16696
PRCC( $F$ ,1 h)	0.12788	0.52405	0.85069	0.68899	-0.35946	-0.55150
PRCC( $A$ ,1 h)	-0.02169	-0.16545	-0.45533	-0.24162	0.08285	0.14085
PRCC( $R$ ,1 h)	0.06123	0.32027	0.72956	0.46364	-0.19797	-0.28509
PRCC( $S$ ,10 h)	-0.36729	-0.27416	-0.40630	-0.34399	0.15168	0.53178
PRCC( $F$ ,10 h)	0.18956	0.49155	0.67193	0.55311	-0.26960	-0.81199
PRCC( $A$ ,10 h)	-0.06678	-0.25292	-0.36120	-0.29522	0.11705	0.42062
PRCC( $R$ ,10 h)	0.13050	0.35427	0.54956	0.43078	-0.19729	-0.69605
PRCC( $S$ ,100 h)	-0.33893	-0.24777	-0.38422	-0.30025	0.12914	0.56675
PRCC( $F$ ,100 h)	0.17244	0.45223	0.63376	0.50030	-0.23642	-0.82047
PRCC( $A$ ,100 h)	-0.06158	-0.17745	-0.25095	-0.20439	0.06632	0.38276
PRCC( $R$ ,100 h)	0.11273	0.30119	0.48277	0.35914	-0.15850	-0.70620
Minimum	0.22	0.007	0.133	0.1	0.1	0.03
Baseline	2.2	0.07	1.33	1	1	0.3
Maximum	6.6	1.4	6.65	5	5	1.5
Parameter	$\sigma_8$	$\sigma_3$	$\sigma_{11}$	$\sigma_6$	$\omega_2$	$\sigma_{12}$
PRCC( $S$ ,0.1 h)	0.00418	0.00133	0.00721	-0.00730	0.00880	-0.00095
PRCC( $F$ ,0.1 h)	0.00491	-0.02376	-0.00479	-0.01447	0.00070	0.00029
PRCC( $A$ ,0.1 h)	0.94584	0.94967	0.43179	-0.14146	-0.02909	0.01632
PRCC( $R$ ,0.1 h)	-0.00100	-0.00278	0.00123	0.00560	0.00341	0.99028

*Continued on next page*

Parameter	$\sigma_8$	$\sigma_3$	$\sigma_{11}$	$\sigma_6$	$\omega_2$	$\sigma_{12}$
PRCC( <i>S</i> ,1 h)	-0.00087	0.00042	-0.00427	0.00687	0.00177	0.00779
PRCC( <i>F</i> ,1 h)	0.00618	-0.00739	0.00563	-0.01924	0.00263	-0.00287
PRCC( <i>A</i> ,1 h)	0.91506	0.83297	0.64729	-0.35019	-0.17798	0.00315
PRCC( <i>R</i> ,1 h)	0.00334	-0.01925	0.00145	0.00094	0.00290	0.71206
PRCC( <i>S</i> ,10 h)	-0.00308	-0.01061	-0.00714	0.00995	-0.01861	0.01484
PRCC( <i>F</i> ,10 h)	0.01215	-0.00269	0.00844	-0.01508	0.00412	-0.01259
PRCC( <i>A</i> ,10 h)	0.88966	0.56291	0.46346	-0.27714	-0.70996	0.00142
PRCC( <i>R</i> ,10 h)	0.01655	-0.01123	0.00754	-0.01035	-0.00245	0.30818
PRCC( <i>S</i> ,100 h)	-0.00690	-0.01292	-0.00574	0.00764	-0.01664	0.01243
PRCC( <i>F</i> ,100 h)	0.01736	0.00037	0.00739	-0.01191	0.00101	-0.01150
PRCC( <i>A</i> ,100 h)	0.81841	0.37472	0.30075	-0.17214	-0.87775	-0.00371
PRCC( <i>R</i> ,100 h)	0.02093	-0.00869	0.00635	-0.01199	-0.00584	0.25393
Minimum	0.00033	0.0111	0.1	0.1	0.002	0.01
Baseline	0.0033	0.111	1	1	0.02	0.1
Maximum	0.99	1.11	5	5	0.2	1
Parameter	$\sigma_{13}$	$\omega_3$				
PRCC( <i>S</i> ,0.1 h)	0.01202	-0.00260				
PRCC( <i>F</i> ,0.1 h)	0.01100	-0.00583				
PRCC( <i>A</i> ,0.1 h)	0.00190	0.00014				
PRCC( <i>R</i> ,0.1 h)	0.84920	-0.25007				
PRCC( <i>S</i> ,1 h)	0.00730	0.00780				
PRCC( <i>F</i> ,1 h)	0.01072	-0.01173				
PRCC( <i>A</i> ,1 h)	0.01013	0.00761				
PRCC( <i>R</i> ,1 h)	0.82148	-0.49732				
PRCC( <i>S</i> ,10 h)	0.00154	0.01567				
PRCC( <i>F</i> ,10 h)	0.00974	-0.01014				
PRCC( <i>A</i> ,10 h)	0.00512	0.01810				
PRCC( <i>R</i> ,10 h)	0.68681	-0.75844				
PRCC( <i>S</i> ,100 h)	-0.00381	0.01276				
PRCC( <i>F</i> ,100 h)	0.01531	-0.00586				
PRCC( <i>A</i> ,100 h)	0.00191	-0.00058				
PRCC( <i>R</i> ,100 h)	0.61909	-0.74965				
Minimum	0.013	0.0139				
Baseline	0.13	0.139				
Maximum	1.3	1.39				

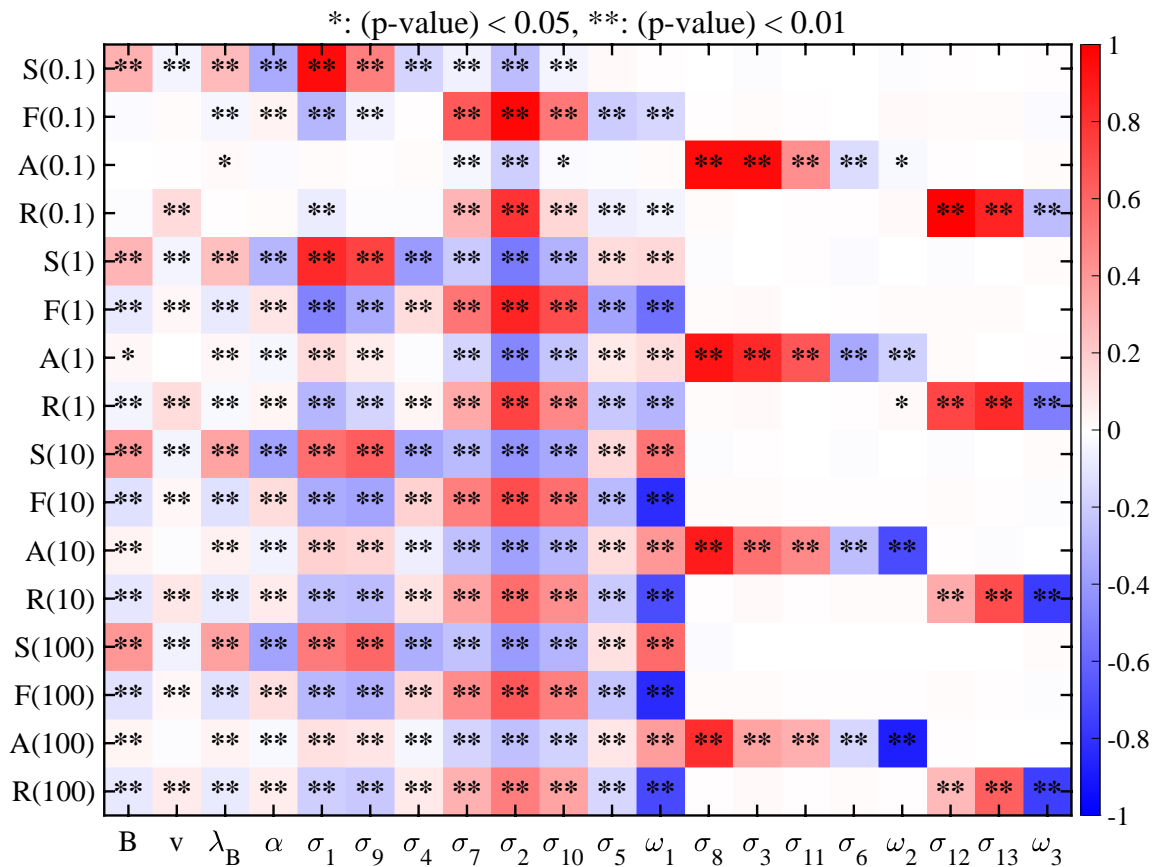


**Figure 7.** Sensitivity analysis: General Latin Hypercube Sampling (LHS) scheme and Partial Rank Correlation Coefficient (PRCC) performed on the model. The colors in each sub box indicated PRCC values of the intracellular molecules carried out using the method of [104] with sample size 10,000.

#### 3.4. Constant sequential administration of bortezomib and OV

To investigate the effect of injection sequence, we consider two administration schedules: (i) Bortezomib + oncolytic-virus (bortezomib first) (Figure 8(A)–(D)) and (ii) oncolytic-virus + Bortezomib (OV first) (Figure 8(E)–(H)). The approach involves partitioning the 30-day interval evenly, allocating 15 days for the first therapeutic administration followed by an additional 15 days for the subsequent treatment. The objective is to discern the therapeutic administration sequence that yields a synergistic effect in the eradication of cancer cells. In these cases, the cumulative amounts of OV and bortezomib are the same ( $\sum_{t=0}^{t=30} u_V = 0.5$  and  $\sum_{t=0}^{t=30} u_B = 0.75$ ). Figure 8(A),(B) show the time courses of injection rate and concentration of OV (red curves) and bortezomib (blue curves) of the case where bortezomib is administered first. Figure 8(C) shows the time courses of intracellular signaling (NF $\kappa$ B ( $F$ ), BAX ( $A$ ), and RIP1 ( $R$ )) in response to bortezomib first administration. Simulations reveal a scenario where cancer cells might elude the apoptotic pathway over the 15-day course of bortezomib administration (as depicted in Figure 8(C)). Notably, the initiation of oncolysis becomes feasible only upon the subsequent

implementation of oncolytic virus therapy (as illustrated in Figure 8(D)). This observation prompted to explore an alternative scenario, involving the administration of oncolytic virus (OV) prior to bortezomib. Figure 8(E),(F) display the time courses of injection rate and concentration of OV (red curves) and bortezomib (blue curves) of the OV first administration. Corresponding time course evolutions of intracellular signaling variables ( $\text{NF}\kappa\text{B}$  ( $F$ ), BAX ( $A$ ), and RIP1 ( $R$ )) are depicted in Figure 8(G). Significantly, the induction of oncolysis ensues as a result of OV administration, subsequently leading to necroptosis following bortezomib administration. Despite the equal administration of OV and bortezomib, distinct profiles emerge within the cancer cell population (depicted in Figure 8(D),(H)) as well as intracellular signaling dynamics (illustrated in Figure 8(C),(G)). In the scenario where bortezomib is administered first, cancer cells can evade the apoptotic phenotype. Conversely, when OV takes precedence in administration before bortezomib, oncolysis followed by necroptosis can be promoted. Consequently, the synergistic effect of these therapeutic agents is achieved by administering OV before bortezomib. However, constant administration of bortezomib and OV, as illustrated in Figure 8, poses challenges within a clinical context, encompassing concerns related to drug toxicity and practical feasibility. Consequently, we intend to explore a scenario in which the administration durations for both OV and bortezomib are confined to a single day, with a sole administration of OV.

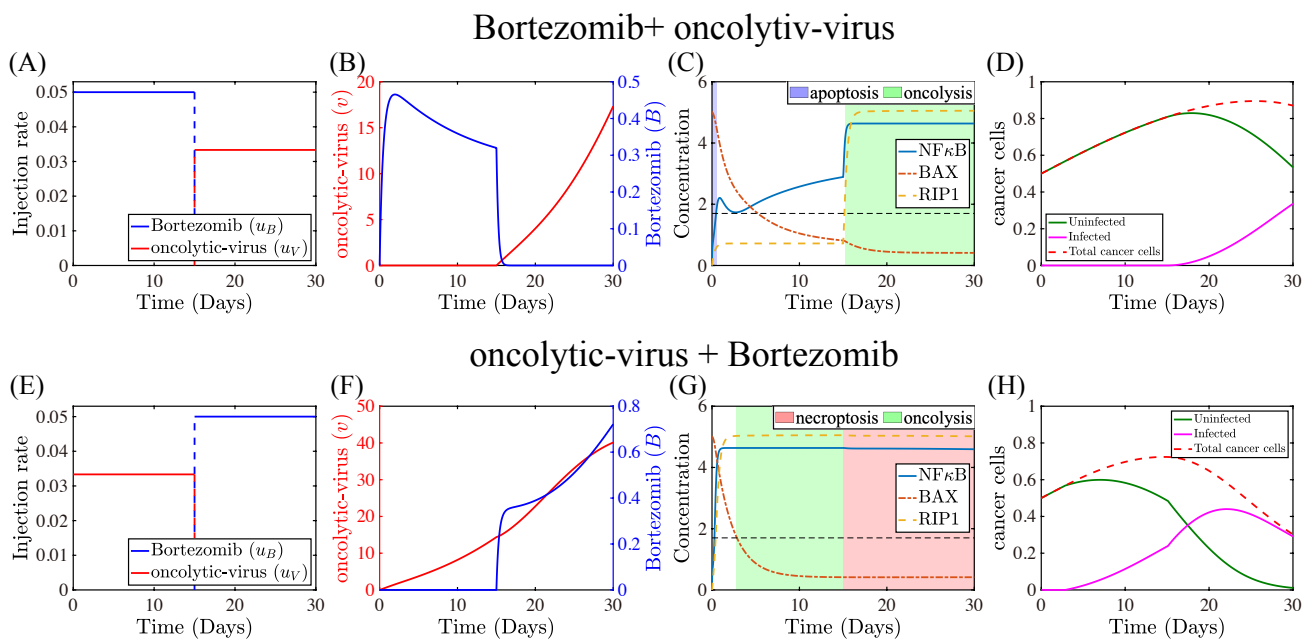


**Figure 8.** The effect of sequential administration of bortezomib and OV on anti-tumor efficacy. (A,B) Time evolution of injection rates ( $u_B, u_V$ ) and concentration of OV ( $v$ ) and bortezomib ( $B$ ) in response to the case where bortezomib is administered first. (C) Time courses of the  $\text{NF}\kappa\text{B}$  ( $F$ ), BAX ( $A$ ), and RIP1 ( $R$ ) in response to the case where bortezomib first administration. (D) Time courses of cancer cells in the response bortezomib first administration. (E,F) Time evolution of injection rates ( $u_B, u_V$ ) and concentration of OV ( $v$ ) and bortezomib ( $B$ ) in response to OV first administration. (G) Time courses of the  $\text{NF}\kappa\text{B}$  ( $F$ ), BAX ( $A$ ), and RIP1 ( $R$ ) in response to OV first administration. (H) Time courses of cancer cells in response to OV is first administration.



We examined a periodic bortezomib administration and a single OV administration within the time interval  $[0, 30]$ . The 30-day duration is partitioned where OV is introduced for a single day, followed by a 14-day interval of rest. Subsequently, the remaining days are divided into five segments, during which bortezomib is administered five times. Given its inherent replication capacity, OV is administered solely on the initial phase within a 15-day interval. We have examined six distinct injection schedules, comprising a single administration of OV and five instances of bortezomib. The total amount of OV and bortezomib is same as in the constant sequential OV and bortezomib administration above. We denote OV and bortezomib as ‘V’ and ‘B’, respectively. For instance, ‘BBBBBV’ reflects five administration of bortezomib within the first 15 days and one time OV administration in the remaining 15 days. Figure 9(A)–(D) show the time courses of injection rates ( $u_B, u_V$ ), concentration of OV and bortezomib, concentration of intracellular signaling variables (NF $\kappa$ B, BAX, and RIP1), and cancer cells (uninfected, infected, and total cancer cells) of the ‘BBBBBV’, respectively. Observe that in Figure 9(C), there are two phenotypes: apoptosis (blue region) and oncolysis (green region). Remarkably, despite employing an equivalent quantity of bortezomib as seen in the constant sequential administration of OV and bortezomib shown in Figure 8, distinct phenotypic outcomes can be elicited. Hence, administering a substantial quantity separately proves more effective than delivering a smaller dose over an extended period. Figure 9(E)–(H) showcase the outcomes for the ‘VBBBBB’ scenario, revealing a clear manifestation of the synergistic effect between OV and bortezomib. Upon each bortezomib injection (from day 15th), a rapid increase in the level of OV becomes evident (depicted in Figure 9(F)). This phenomenon arises from the combined action of OV and bortezomib treatment, which induces a necroptotic phenotype and consequently enhances viral infections. As a result, the replication term (second term in Eq (2.8)) contributes to the substantial increase in OV levels. In Figure 9(G), a distinct alternation between necroptosis and oncolysis emerges starting at the 15-day mark, coinciding with bortezomib injections. However, the discernible effect on the cancer cell population remains limited, primarily attributed to the supplementary role played by bortezomib, which acts as an enhancer, while OV alone displays only modest infectivity towards cancer cells (as demonstrated in Figures 8(H) and 9(H)). In the context of single administering OV and five bortezomib injections, an intriguing query arises: Should the OV injection be administered solely at the beginning or the end of bortezomib administration? To address this concern, we strategically place the OV injection between the bortezomib administrations. The temporal dynamics of phenotypic changes corresponding to diverse injection schedules are illustrated in Figure 9(I). Figure 9(I) illustrates the discrete phenotypic states of cancer cells resulting from various injection schedules. Figure 9(J) displays the normalized cancer cell (green: uninfected cancer cells; pink: infected cancer cells; red: total cancer cells (uninfected + infected)) outcomes across all scenarios at the final time point. Evidently, the ‘BBBBBV’ scenario exhibits the least effectiveness in eradicating cancer cells. Conversely, the ‘VBBBBB’ scenario emerges as the most potent in targeting uninfected cancer cells for elimination. Generally, the strategy commencing with OV demonstrates a superior anti-cancer effect compared to the approach initiated with bortezomib. Nonetheless, an important query arises regarding the optimality of the strategy derived from these findings. Up to this point, the injection timings have been manually set, and the cumulative dosage of anti-cancer drugs has been predetermined. Furthermore, it’s noteworthy that the bortezomib dosage surpasses our reference threshold of 1, consequently impacting patient toxicity levels.

As a result, the subsequent section will elucidate how the application of optimal control theory can

yield favorable outcomes, further utilizing minimal quantities of OV and bortezomib.

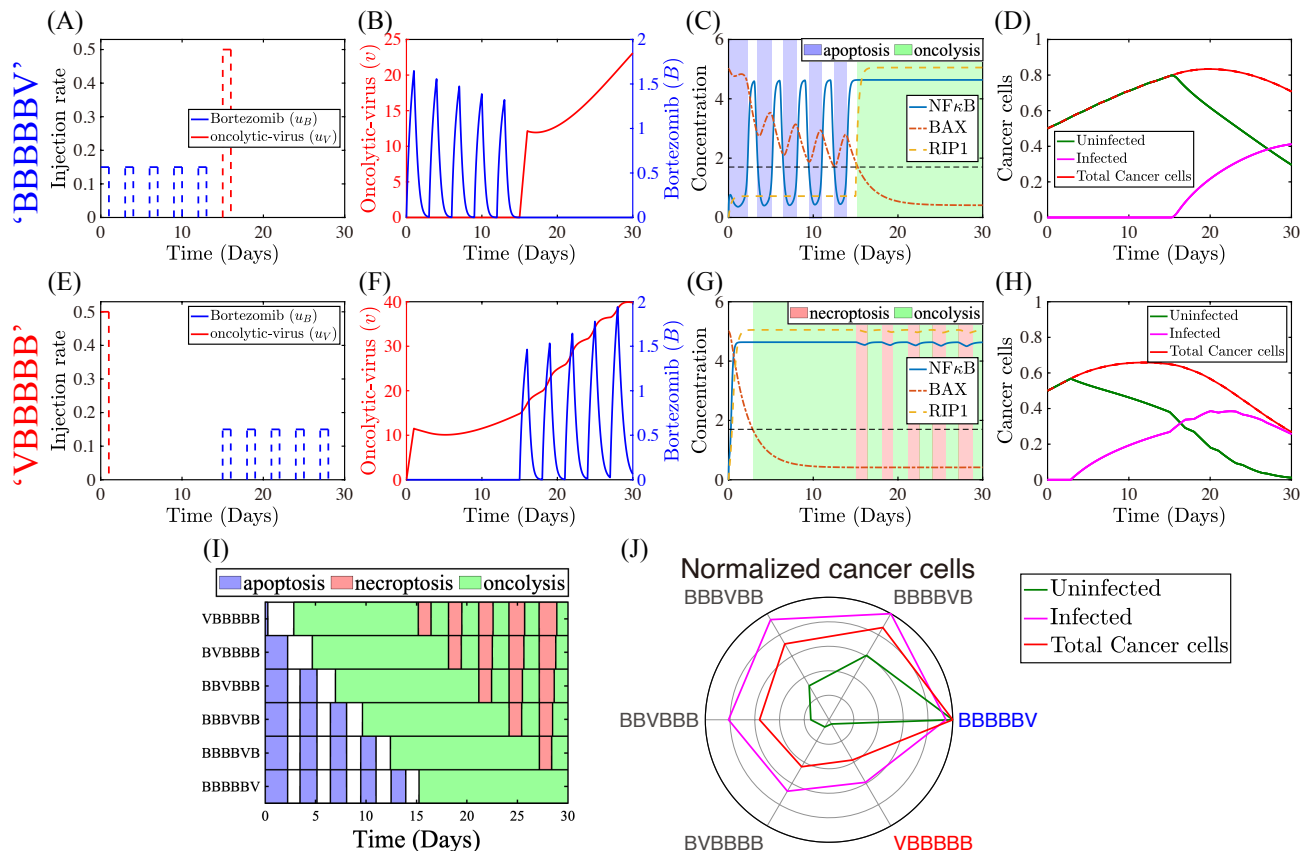


**Figure 9.** Dynamics of the system corresponding to vary alternating schemes of bortezomib and OV. (A,B) Time evolution of injection rate ( $u_B, u_V$ ) and concentration of OV ( $v$ ) and bortezomib ( $B$ ) in the response to the case where bortezomib is injected first. (C) Time courses of the NF $\kappa$ B ( $F$ ), BAX ( $A$ ), and RIP1 ( $R$ ) in response to the case where bortezomib is injected first. (D) Time courses of cancer cells in the response to the case where bortezomib is injected first. (E,F) Time evolution of injection rate ( $u_B, u_V$ ) and concentration of OV ( $v$ ) and bortezomib ( $B$ ) in the response to the case where OV is injected first. (G) Time courses of the NF $\kappa$ B ( $F$ ), BAX ( $A$ ), and RIP1 ( $R$ ) in response to the case where OV is injected first. (H) Time courses of cancer cells in the response to the case where OV is injected first. (I) Time courses of changing phenotype. (J) Normalized cancer cells at final time for various injection schedules.

### 3.5. Optimal administration of OV and bortezomib

Now, we investigate the optimal control problems for various objective functions in Eqs (2.12) and (2.13). As observed from the previous results, it is evident that administering OV first is significantly more effective compared to administering bortezomib first. The simulation outcomes and analysis support the idea that initiating the treatment with OV leads to superior therapeutic results in combating cancer progression and inducing necroptotic phenotype. This finding can have important implications for designing optimized treatment strategies in clinical settings, prioritizing OV administration for improved efficacy and better patient outcomes. Regarding the objective function, as described in the

previous section, we will examine the following results using two different objective functions (Eqs (2.12) and (2.13)). Each objective function represents a distinct therapeutic goal, and by analyzing the outcomes based on these different criteria, we aim to gain comprehensive insights into the effectiveness of the treatment strategies in different scenarios. These objective functions allow us to assess the impact of the interventions from multiple perspectives, providing a more comprehensive evaluation of the treatment outcomes.

### 1) Quadratic controls

In this therapeutic strategy, we investigate the optimal control problem for objective function Eq (2.12). Figure 10(A),(B) shows the time courses of the injection rate and concentration of OV and bortezomib, respectively. We set that the state stays at necroptotic phenotype after injecting bortezomib (day 15th). That is, the level of bortezomib never falls under the threshold ( $th_B = 0.1$ ). In Figure 9(G), necroptotic and oncolytic mode alternately appeared even though the total amount of bortezomib is 0.75. However, with the application of optimal control theory, necroptotic phenotype is maintained from the moment bortezomib is injected (Figure 10(C)). It is worth noting that with optimal control, total amount of bortezomib is just 0.6733. Because we set the upper bound of the control when applying the optimal control theory, the level of bortezomib does not exceed the reference value (Figure 10(B)). However, in this case, one-time OV is coupled with frequent bortezomib administrations, the inconvenience arises from the need for repetitive hospital visits solely for the purpose of bortezomib injections. Hence, we present an alternative approach, incorporating intervals of respite between bortezomib injections (depicted in Figure 10(E)–(H)). This strategy involves a one-time OV coupled with intermittent bortezomib administration. In this latter scenario, the injection intervals are designed, ensuring that the bortezomib dosage threshold will not be exceeded that could potentially lead to toxicity. The total amount of bortezomib, in this case, is calculated at 0.2823, significantly lower by over fifty percent compared to the previous scenario's value of 0.6733. Furthermore, there is a notable reduction in the total amount of OV, diminishing from 0.5 as seen in Figures 8 and 9, to 0.2938 as demonstrated in Figure 10. In the second scenario, the injection strategy of bortezomib shows four injections in 15 days. The possible actual administration of bortezomib could be bolus intravenous injection twice weekly for two weeks (days 1, 4, 8, and 11) followed by a ten-day rest period [105, 106]. Hence, our mathematical model utilizing optimal control theory, aligns with the practical drug administration protocols and has the potential to provide valuable insights into optimizing drug utilization within real treatment scenarios.

### 2) Linear controls with constraint

In this therapeutic approach, we consider the impact of initially administering OV followed by bortezomib, employing a sigmoid function to effectively steer cells toward a necroptotic phenotype. We divided the entire time into two periods: the period of injecting only OV and the period of injecting only bortezomib. In the first integration term (in Eq (2.13)), a term for uninfected cancer cells ( $x(t)$ ) is added because the main purpose is to infect cancer cells through OV. The objective function of the second integration term (in Eq (2.13)) considers a sigmoid term for bortezomib to keep the cells in the necroptotic phenotype. Figure 11 are the results for Eq (2.13). Figure 11(A),(B) shows the time courses of injection rate ( $u_V$  and  $u_B$ ) and concentration of OV ( $v$ ) and bortezomib ( $B$ ), respectively. Figure 11(C),(D) illustrate the time courses of intracellular signaling (NF $\kappa$ B, BAX, RIP1) and cancer cell population (uninfected, infected, and total cancer cells), respectively.

Bortezomib continues to maintain a level that satisfies the necroptotic phenotype (blue curves in Figure 11(B)). As a result, after 15 days, the necroptosis phenotype is maintained and more cancer cells can be infected (Figure 11(C),(D)). The mechanism of quadratic controls necessitates the dynamic adjustment of infusion rates over time, as both  $u_V$  and  $u_B$  exhibit continuous dynamics when the necessary conditions for optimal control are computed. In contrast, linear controls result to either 0 or the maximum injection rate which is due to the calculation of necessary conditions in the optimal control formulation. Consequently, linear controls provide practical administration protocol as it do not require temporal adjustments to the injection rate.

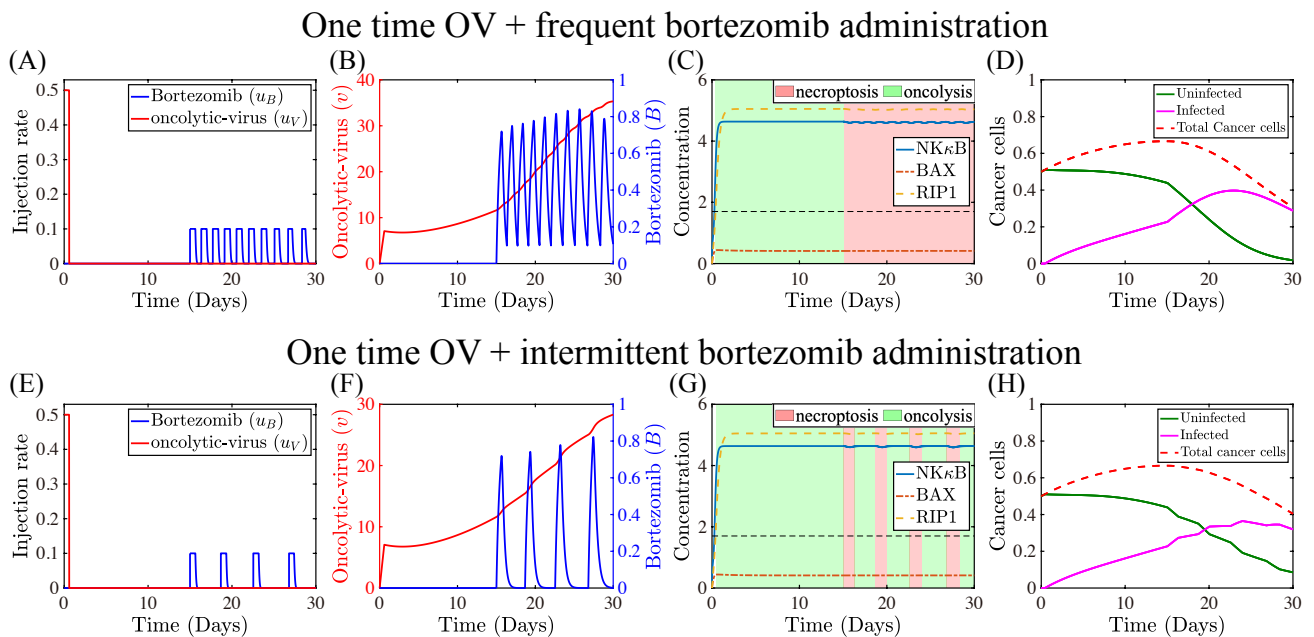


**Figure 10.** Dynamics of the system corresponding to the OV first schemes with quadratic controls. (A,E) Time courses of injection rate of OV and bortezomib. (B,F) Time courses of concentration of OV and bortezomib. (C,G) Time courses of the intracellular modules (NF $\kappa$ B (F), BAX (A), and RIP1 (R)). (D,H) Time courses of the cancer cell population (uninfected, infected, and total cancer cells).

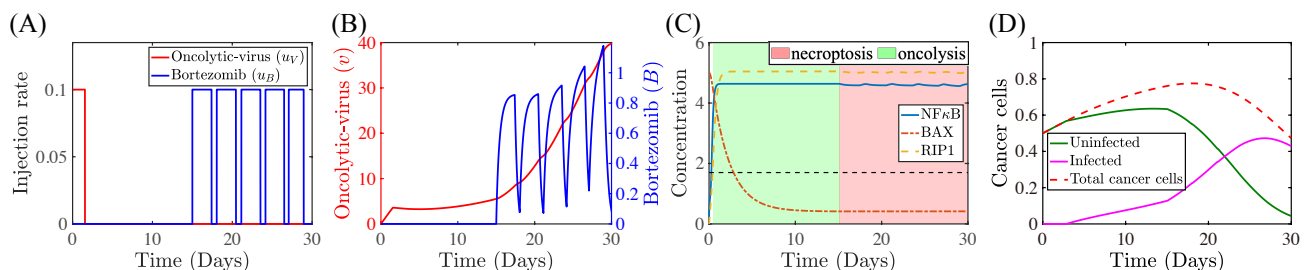


**Figure 11.** Dynamics of the system corresponding to two schemes of bortezomib and OV with linear control. (A,B,C,D) Time courses of the injection rate ( $u_V$ ,  $u_B$ ), concentration of OV and bortezomib, intracellular signaling (NF $\kappa$ B, BAX, RIP1), and cancer cell population (uninfected, infected, and total cancer cells), respectively.

## 4. Discussion

The optimal control framework herein is based on the mathematical models developed by [45, 46] describing the intracellular dynamics and tumor suppression in response to a combination therapy involving bortezomib and OV in cancer patients. While bortezomib is quite effective in killing cancer cells in general, it can cause strong toxicity and serious side effects. One of our goals of this study is to analyze the cellular system behaviors in response to bortezomib-OV combination therapy via a delicate intracellular signaling pathway (NF $\kappa$ B-Bcl-2-BAX-RIP1). Another goal is to find optimal strategies that effectively kill cancer cells by OV and bortezomib through both apoptotic and necroptotic phenotype with minimal costs (side effects + administrative costs) using optimal control theory [46]. The associated optimal control problems are formulated such that the overall cancer cell population and the total cost of the two anticancer drugs are minimized.

Yoo et al. showed that OV replication, thus anti-tumor efficacy, can be improved by the unfolded protein response (UPR) after bortezomib treatment, inducing synergistic cancer cell killing [6]. Kim et al. [46] introduced the apoptosis and necroptosis cell death mechanism involved in this combination (OV + bortezomib) therapy. In this work, a detailed analysis of the model in this work suggests that injection of OVs followed by bortezomib can effectively increase anti-tumor efficacy due to the higher infection rate of cancer cells from the oncolytic mode and superior killing capacity of tumor cells from combined cell death (necroptosis + oncolysis) phase while the OV treatment at a latter time induces only oncolysis or a mild killing phase (apoptosis + oncolysis), leading to lower killing rates (Figures 8 and 9). Treatment of a tumor with OVs at an earlier time usually leads to better anti-tumor efficacy [6] and our study supports the idea of effectiveness of initial OV treatment even in the combination therapy by revealing the dynamics of detailed sub-cellular cell death program at an intracellular level. Relative order of OVs relative to bortezomib treatment in a combination therapy induces the cellular transition from the severe ON (oncolysis + necroptosis) mode to the intermediate AON phase (apoptosis + oncolysis + necroptosis), and to mild AO (apoptosis + oncolysis) phase (Figure 9). Therefore, delays in OV treatment decrease anti-tumor efficacy, suggesting the importance of OV injection time. Excessive use of OVs and bortezomib also has to be limited due to safety issues and drug-associated side effects, respectively, in addition to a need to minimize administrative costs. Anti-cancer strategies with optimal control in our work suggest that both the necroptosis-dominant phase from frequent injection of bortezomib and a mixed (necroptosis + oncolysis) mode from less frequent injection mode of bortezomib can effectively kill cancer cells in the 2nd cell death program a combination therapy with initial administration of OVs (Figures 10 and 11). Optimally controlled injection strategy of OVs and bortezomib in this work may lead to better understanding of fundamental mechanisms of the cell death program and effective anti-cancer efficacy in various cancers [105, 106].

### Use of AI tools declaration

The authors declare they have not used Artificial Intelligence (AI) tools in the creation of this article.

### Acknowledgments

This work was supported by the National Research Foundation of Korea (NRF) grant funded by the Korea government (MSIT) (No. NRF-2021R1A2C1010891) (Y.K.).

## Conflict of interest

The authors declare there is no conflict of interest.

## References

1. K. Aldape, K. Brindle, L. Chesler, R. Chopra, A. Gajjar, M. Gilbert, et al., Challenges to curing primary brain tumours, *Nat. Rev. Clin. Oncol.*, **16** (2019), 509–520. <https://doi.org/10.1038/s41571-019-0177-5>
2. J. Godlewski, M. Nowicki, A. Bronisz, G. N. J. Palatini, M. D. Lay, J. Brocklyn, et al., MicroRNA-451 regulates LKB1/AMPK signaling and allows adaptation to metabolic stress in glioma cells, *Mol. Cell*, **37** (2010), 620–632. <https://doi.org/10.1016/j.molcel.2010.02.018>
3. J. Lee, J. Kim, Y. Kim, Atorvastatin-mediated rescue of cancer-related cognitive changes in combined anticancer therapies, *PLoS Comput. Biol.*, **17** (2021), e1009457. <https://doi.org/10.1371/journal.pcbi.1009457>
4. S. Schagen, A. Tsvetkov, A. Compter, J. Wefel, Cognitive adverse effects of chemotherapy and immunotherapy: are interventions within reach?, *Nat. Rev. Neurol.*, **18** (2022), 173–185. <https://doi.org/10.1038/s41582-021-00617-2>
5. L. Zhong, Y. Li, L. Xiong, W. Wang, M. Wu, T. Yuan, et al., Small molecules in targeted cancer therapy: advances, challenges, and future perspectives, *Signal Transduction Targeted Ther.*, **6** (2021), 201. <https://doi.org/10.1038/s41392-021-00572-w>
6. J. Yoo, B. Hurwitz, C. Bolyard, J. Yu, J. Zhang, K. Selvendiran, et al., Bortezomib-induced unfolded protein response increases oncolytic hsv-1 replication resulting in synergistic antitumor effects, *Clin. Cancer Res.*, **20** (2014), 3787–3798. <https://doi.org/10.1158/1078-0432.CCR-14-0553>
7. M. A. Shahshahan, M. N. Beckley, A. R. Jazirehi, Potential usage of proteasome inhibitor bortezomib (Velcade, PS-341) in the treatment of metastatic melanoma: Basic and clinical aspects, *Am. J. Cancer Res.*, **1** (2011), 913–924.
8. B. Cvek, Z. Dvorak, The ubiquitin-proteasome system (UPS) and the mechanism of action of bortezomib, *Curr. Pharm. Des.*, **17** (2011), 1483–1499. <https://doi.org/10.2174/138161211796197124>
9. B. A. Teicher, J. E. Tomaszewski, Proteasome inhibitors, *Biochem. Pharmacol.*, **96** (2015), 1–9. <https://doi.org/10.1016/j.bcp.2015.04.008>
10. N. Rastogi, D. P. Mishra, Therapeutic targeting of cancer cell cycle using proteasome inhibitors, *Cell Div.*, **7** (2012), 26. <https://doi.org/10.1186/1747-1028-7-26>
11. D. Chen, M. Frezza, S. Schmitt, J. Kanwar, Q. Dou, Bortezomib as the first proteasome inhibitor anticancer drug: current status and future perspectives, *Curr. Cancer Drug Targets*, **11** (2011), 239–253. <https://doi.org/10.2174/156800911794519752>
12. J. Z. Qin, H. Xin, L. A. Sitailo, M. F. Denning, B. J. Nickoloff, Enhanced killing of melanoma cells by simultaneously targeting Mcl-1 and NOXA, *Cancer Res.*, **66** (2006), 9636–9645. <https://doi.org/10.1158/0008-5472.CAN-06-0747>

13. A. Dudek, K. Lesniewski-Kmak, N. Shehadeh, O. Pandey, M. Franklin, R. Kratzke, et al., Phase I study of bortezomib and cetuximab in patients with solid tumours expressing epidermal growth factor receptor, *Br. J. Cancer*, **100** (2009), 1379–1384. <https://doi.org/10.1038/sj.bjc.6605043>
14. J. Gilbert, J. W. Lee, A. Argiris, M. Haigentz, L. E. Feldman, M. Jang, et al., Phase II 2-arm trial of the proteasome inhibitor, PS-341 (bortezomib) in combination with irinotecan or PS-341 alone followed by the addition of irinotecan at time of progression in patients with locally recurrent or metastatic squamous cell carcinoma of the head and neck (e1304): A trial of the eastern cooperative oncology group, *Head Neck*, **35** (2013), 942–948. <https://doi.org/10.1002/hed.23046>
15. C. Colomer, L. Marruecos, A. Vert, A. Bigas, L. Espinosa, Nf-kb members left home: Nf-kb-independent roles in cancer, *Biomedicines*, **5** (2017), 26. <https://doi.org/10.3390/biomedicines5020026>
16. K. Campbell, S. Tait, Targeting BCL-2 regulated apoptosis in cancer, *Open Biol.*, **8** (2018), 180002.
17. D. Westphal, R. Kluck, G. Dewson, Building blocks of the apoptotic pore: how bax and bak are activated and oligomerize during apoptosis, *Cell Death Differ.*, **21** (2014), 196–205. <https://doi.org/10.1038/cdd.2013.139>
18. N. Mitsiades, C. Mitsiades, V. Poulaki, D. Chauhan, P. Richardson, T. Hideshima, et al., Biologic sequelae of nuclear factor-kappa B blockade in multiple myeloma: therapeutic applications, *Blood*, **29** (2002), 4079–4086. <https://doi.org/10.1182/blood.V99.11.4079>
19. P. Richardson, T. Hideshima, K. Anderson, Bortezomib (PS-341): a novel, first-in-class proteasome inhibitor for the treatment of multiple myeloma and other cancers, *Cancer Control*, **10** (2003), 361–369. <https://doi.org/10.1177/107327480301000502>
20. A. Ashkenazi, G. Salvesen, Regulated cell death: signaling and mechanisms, *Annu. Rev. Cell Dev. Biol.*, **30** (2014), 337–356. <https://doi.org/10.1146/annurev-cellbio-100913-013226>
21. K. Brown, S. Park, T. Kanno, G. Franzoso, U. Siebenlist, Mutual regulation of the transcriptional activator nf-kappa B and its inhibitor, I kappa B-alpha., *PNAS*, **90** (1993), 2532–2536. <https://doi.org/10.1073/pnas.90.6.2532>
22. P. Fan, A. Tyagi, F. Agboke, R. Mathur, N. Pokharel, V. Jordan, Modulation of nuclear factor-kappa B activation by the endoplasmic reticulum stress sensor PERK to mediate estrogen-induced apoptosis in breast cancer cells, *Cell Death Discovery*, **4** (2018), 15. <https://doi.org/10.1038/s41420-017-0012-7>
23. M. Ma, K. Parker, S. Manyak, C. Altamirano, Z. Wu, M. J. Borad, J. R. Berenson, Proteasome inhibitor PS-341 markedly enhances sensitivity of multiple myeloma cells to chemotherapeutic agents and overcomes chemoresistance through inhibition of the NF-kappa B pathway, *Blood*, **98** (2001), 473a.
24. J. Berenson, H. Ma, R. Vescio, The role of nuclear factor-kappa B in the biology and treatment of multiple myeloma, *Semin. Oncol.*, **28** (2001), 626–633. [https://doi.org/10.1016/S0093-7754\(01\)90036-3](https://doi.org/10.1016/S0093-7754(01)90036-3)
25. A. Masilamani, R. Ferrarese, E. Kling, N. Thudi, H. Kim, D. Scholtens, et al., KLF6 depletion promotes nf-kb signaling in glioblastoma, *Oncogene*, **36** (2017), 3562–3575. <https://doi.org/10.1038/onc.2016.507>

26. M. Karin, Nuclear factor-kappaB in cancer development and progression, *Nature*, **441** (2006), 431–436. <https://doi.org/10.1038/nature04870>
27. T. Strobel, Y. Tai, S. Korsmeyer, S. Cannistra, Bad partly reverses paclitaxel resistance in human ovarian cancer cells, *Oncogene*, **17** (1998), 2419–2427. <https://doi.org/10.1038/sj.onc.1202180>
28. J. Wojton, W. Meisen, B. Kaur, How to train glioma cells to die: molecular challenges in cell death, *J. Neuro-Oncol.*, **126** (2016), 377–384. <https://doi.org/10.1007/s11060-015-1980-1>
29. M. Rosenfeld, X. Ye, J. Supko, S. Desideri, S. Grossman, S. Brem, et al., A phase I/II trial of hydroxychloroquine in conjunction with radiation therapy and concurrent and adjuvant temozolomide in patients with newly diagnosed glioblastoma multiforme, *Autophagy*, **10** (2014), 1359–1368. <https://doi.org/10.4161/auto.28984>
30. S. Melo-Lima, M. C. Lopes, F. Mollinedo, Necroptosis is associated with low procaspase-8 and active RIPK1 and -3 in human glioma cells, *Oncoscience*, **1** (2014), 649–664. <https://doi.org/10.18632/oncoscience.89>
31. S. Russell, J. Bell, C. Engeland, G. McFadden, Advances in oncolytic virotherapy, *Commun. Med.*, **2** (2022), 33. <https://doi.org/10.1038/s43856-022-00098-4>
32. J. Malinzi, R. Ouifki, A. Eladdadi, D. F. M. Torres, K. A. J. White, Enhancement of chemotherapy using oncolytic virotherapy: Mathematical and optimal control analysis, *Math. Biosci. Eng.*, **15** (2018), 1435–1463. <https://doi.org/10.3934/mbe.2018066>
33. E. Kelly, S. J. Russell, History of oncolytic viruses: Genesis to genetic engineering, *Mol. Ther.*, **15** (2007), 651–659. <https://doi.org/10.1038/sj.mt.6300108>
34. H. Fukuhara, Y. Ino, T. Todo, Oncolytic virus therapy: A new era of cancer treatment at dawn, *Cancer Sci.*, **107** (2016), 1373–1379. <https://doi.org/10.1111/cas.13027>
35. E. A. Chiocca, S. D. Rabkin, Oncolytic viruses and their application to cancer immunotherapy, *Cancer Immunol. Res.*, **2** (2014), 295–300. <https://doi.org/10.1158/2326-6066.CIR-14-0015>
36. D. Shin, T. Nguyen, B. Ozpolat, F. Lang, M. Alonso, C. Gomez-Manzano, et al., Current strategies to circumvent the antiviral immunity to optimize cancer virotherapy, *J. ImmunoTher. Cancer*, **9** (2021), e002086. <https://doi.org/10.1136/jitc-2020-002086>
37. A. Nguyen, L. Ho, Y. Wan, Chemotherapy and oncolytic virotherapy: advanced tactics in the war against cancer, *Front. Oncol.*, **4** (2014), 145. <https://doi.org/10.3389/fonc.2014.00145>
38. Y. Kim, H. Lee, N. Dmitrieva, J. Kim, B. Kaur, A. Friedman, Choindroitinase ABC I-mediated enhancement of oncolytic virus spread and anti-tumor efficacy: A mathematical model, *PLoS One*, **9** (2014), e102499. <https://doi.org/10.1371/journal.pone.0102499>
39. R. Kanai, H. Wakimoto, T. Cheema, S. D. Rabkin, Oncolytic herpes simplex virus vectors and chemotherapy: are combinatorial strategies more effective for cancer?, *Future Oncol.*, **6** (2010), 619–634. <https://doi.org/10.2217/fon.10.18>
40. G. Marelli, A. Howells, N. Lemoine, Y. Wang, Oncolytic viral therapy and the immune system: A double-edged sword against cancer, *Front. Immunol.*, **9** (2018), 866. <https://doi.org/10.3389/fimmu.2018.00866>



41. T. C. Liu, E. Galanis, D. Kirn, Clinical trial results with oncolytic virotherapy: a century of promise, a decade of progress, *Nat. Clin. Pract. Oncol.*, **4** (2007), 101–117. <https://doi.org/10.1038/ncponc0736>
42. G. Simpson, K. Relph, K. Harrington, A. Melcher, H. Pandha, Cancer immunotherapy via combining oncolytic virotherapy with chemotherapy: recent advances, *Oncolytic Virother.*, **5** (2016), 1–13.
43. J. Yoo, A. Jaime-Ramirez, C. Bolyard, H. Dai, T. Nallanagulagari, J. Wojton, et al., Bortezomib treatment sensitizes oncolytic HSV-1 treated tumors to NK cell immunotherapy, *Clin. Cancer Res.*, **22** (2016), 5265–5276. <https://doi.org/10.1158/1078-0432.CCR-16-1003>
44. A. Najafov, H. Chen, J. Yuan, Necroptosis and cancer, *Trends Cancer*, **3** (2017), 294–301. <https://doi.org/10.1016/j.trecan.2017.03.002>
45. Y. Kim, J. Y. Yoo, T. J. Lee, J. Liu, J. Yu, M. A. Caligiuri, et al., Complex role of NK cells in regulation of oncolytic virus-bortezomib therapy, *PNAS*, **115** (2018), 4927–4932. <https://doi.org/10.1073/pnas.1715295115>
46. Y. Kim, J. Lee, D. Lee, H. Othmer, Synergistic effects of bortezomib-OV therapy and anti-invasive strategies in glioblastoma: a mathematical model, *Cancers*, **11** (2019), 215. <https://doi.org/10.3390/cancers11020215>
47. A. Aspirin, A. de Los Reyes, Y. Kim, Polytherapeutic strategies with oncolytic virus-bortezomib and adjuvant NK cells in cancer treatment, *J. R. Soc. Interface*, **18** (2021), 20200669. <https://doi.org/10.1098/rsif.2020.0669>
48. A. Alsisi, R. Eftimie, D. Trucu, Nonlocal multiscale modelling of tumour-oncolytic viruses interactions within a heterogeneous fibrous/non-fibrous extracellular matrix, *Math. Biosci. Eng.*, **19** (2022), 6157–6185. <https://doi.org/10.3934/mbe.2022288>
49. Z. Parra-Guillen, T. Freshwater, Y. Cao, K. Mayawala, S. Zalba, M. Garrido, et al., Mechanistic modeling of a novel oncolytic virus, v937, to describe viral kinetic and dynamic processes following intratumoral and intravenous administration, *Front. Pharmacol.*, **12** (2021), 705443.
50. P. Pooladvand, C. Yun, A. Yoon, P. Kim, F. Frascoli, The role of viral infectivity in oncolytic virotherapy outcomes: A mathematical study, *Math. Biosci.*, **334** (2021), 108520. <https://doi.org/10.1016/j.mbs.2020.108520>
51. N. Almualllem, D. Trucu, R. Eftimie, Oncolytic viral therapies and the delicate balance between virus-macrophage-tumour interactions: A mathematical approach, *Math. Biosci. Eng.*, **18** (2020), 764–799. <https://doi.org/10.3934/mbe.2021041>
52. T. Alzahrani, R. Eftimie, D. Trucu, Multiscale moving boundary modelling of cancer interactions with a fusogenic oncolytic virus: The impact of syncytia dynamics, *Math. Biosci.*, **323** (2020), 108296. <https://doi.org/10.1016/j.mbs.2019.108296>
53. A. Jenner, C. Yun, P. Kim, A. Coster, Mathematical modelling of the interaction between cancer cells and an oncolytic virus: Insights into the effects of treatment protocols, *Bull. Math. Biol.*, **80** (2018), 1615–1629. <https://doi.org/10.1007/s11538-018-0424-4>
54. P. Kim, J. Crivelli, I. Choi, C. Yun, J. Wares, Quantitative impact of immunomodulation versus oncolysis with cytokine-expressing virus therapeutics, *Math. Biosci. Eng.*, **12** (2015), 841–858.

55. A. Jenner, C. Yun, A. Yoon, A. Coster, P. Kim, Modelling combined virotherapy and immunotherapy: strengthening the antitumour immune response mediated by IL-12 and GM-CSF expression, *Lett. Biomath.*, **5** (2018), 99–116.
56. J. Wares, J. Crivelli, C. Yun, I. Choi, J. Gevertz, P. Kim, Treatment strategies for combining immunostimulatory oncolytic virus therapeutics with dendritic cell injections, *Math. Biosci. Eng.*, **12** (2015), 1237–1256. <https://doi.org/10.3934/mbe.2015.12.1237>
57. A. Friedman, J. Tian, G. Fulci, E. Chiocca, J. Wang, Glioma virotherapy: effects of innate immune suppression and increased viral replication capacity, *Cancer Res.*, **66** (2006), 2314–2319. <https://doi.org/10.1158/0008-5472.CAN-05-2661>
58. A. Friedman, X. Lai, Combination therapy for cancer with oncolytic virus and checkpoint inhibitor: A mathematical model, *PLoS One*, **13** (2018), e0192449. <https://doi.org/10.1371/journal.pone.0192449>
59. Y. Otani, D. Bottino, N. Gupta, M. Vakilynejad, Y. Tanigawara, Mathematical models for early detection of relapse in multiple myeloma patients treated with bortezomib/lenalidomide/dexamethasone, *Blood*, **140** (2022), 4310–4311. <https://doi.org/10.1182/blood-2022-157625>
60. L. Zhang, D. Mager, Systems modeling of bortezomib and dexamethasone combinatorial effects on bone homeostasis in multiple myeloma patients, *J. Pharm. Sci.*, **108** (2019), 732–740. <https://doi.org/10.1016/j.xphs.2018.11.024>
61. P. Bloomingdale, C. Meregalli, K. Pollard, A. Canta, A. Chiorazzi, G. Fumagalli, et al., Systems pharmacology modeling identifies a novel treatment strategy for bortezomib-induced neuropathic pain, *Front. Pharmacol.*, **12** (2022), 817236. <https://doi.org/10.3389/fphar.2021.817236>
62. S. Lenhart, J. T. Workman, *Optimal Control Applied to Biological Models*, Chapman & Hall/CRC Mathematical and Computational Biology, Chapman and Hall/CRC, 2007.
63. A. Jarrett, D. Faghihi, D. Ii, E. Lima, J. Virostko, G. Biros, et al., Optimal control theory for personalized therapeutic regimens in oncology: Background, history, challenges, and opportunities, *J. Clin. Med.*, **9** (2020), 1314. <https://doi.org/10.3390/jcm9051314>
64. K. Bahrami, M. Kim, Optimal control of multiplicative control systems arising from cancer therapy, *IEEE Trans. Autom. Control*, **20** (1975), 537–542. <https://doi.org/10.1109/TAC.1975.1101019>
65. G. W. Swan, T. L. Vincent, Optimal control analysis in the chemotherapy of igg multiple myeloma, *Bull. Math. Biol.*, **39** (1977), 317–337. <https://doi.org/10.1007/BF02462912>
66. G. W. Swan, Optimal control applications in the chemotherapy of multiple myeloma, *Math. Med. Biol.: J. IMA*, **2** (1985), 139–160. <https://doi.org/10.1093/imammb/2.3.139>
67. A. Ergun, K. Camphausen, L. Wein, Optimal scheduling of radiotherapy and angiogenic inhibitors, *Bull. Math. Biol.*, **65** (2003), 407–424. [https://doi.org/10.1016/S0092-8240\(03\)00006-5](https://doi.org/10.1016/S0092-8240(03)00006-5)
68. E. Ratajczyk, U. Ledzewicz, H. Schattler, Optimal control for a mathematical model of glioma treatment with oncolytic therapy and tnf- $\alpha$  inhibitors, *J. Optim. Theory Appl.*, **176** (2018), 456–477. <https://doi.org/10.1007/s10957-018-1218-4>

69. H. Schattler, Y. Kim, U. Ledzewicz, A. los Reyes, E. Jung, On the control of cell migration and proliferation in glioblastoma, in *52nd IEEE Conference on Decision and Control*, (2013), 1810–1815. <https://doi.org/10.1109/CDC.2013.6760145>
70. E. Jung, A. los Reyes, K. Pumares, Y. Kim, Strategies in regulating glioblastoma signaling pathways and anti-invasion therapy, *PLoS One*, **14** (2019), e0215547. <https://doi.org/10.1371/journal.pone.0215547>
71. A. L. Reyes, E. Jung, Y. Kim, Optimal control strategies of eradicating invisible glioblastoma cells after conventional surgery, *J. R. Soc. Interface*, **12** (2015), 20141392. <https://doi.org/10.1098/rsif.2014.1392>
72. A. Reyes, Y. Kim, Optimal regulation of tumour-associated neutrophils in cancer progression, *R. Soc. Open Sci.*, **9** (2022), 210705. <https://doi.org/10.1098/rsos.210705>
73. J. Lee, D. Lee, Y. Kim, Mathematical model of stat signalling pathways in cancer development and optimal control approaches, *R. Soc. Open Sci.*, **8** (2021), 210594. <https://doi.org/10.1098/rsos.210594>
74. C. Silva, C. Cruz, D. Torres, A. Munuzuri, A. Carballosa, I. Area, et al., Optimal control of the covid-19 pandemic: controlled sanitary deconfinement in portugal, *Sci. Rep.*, **11** (2021), 3451. <https://doi.org/10.1038/s41598-021-83075-6>
75. I. Ahn, S. Heo, S. Ji, K. Kim, T. Kim, E. Lee, et al., Investigation of nonlinear epidemiological models for analyzing and controlling the mers outbreak in Korea, *J. Theor. Biol.*, **437** (2018), 17–28. <https://doi.org/10.1016/j.jtbi.2017.10.004>
76. U. Ledzewicz, H. Schattler, The structure of optimal protocols for a mathematical model of chemotherapy with antiangiogenic effects, *SIAM J. Control. Optim.*, **60** (2022), 1092–1116. <https://doi.org/10.1137/21M1395326>
77. U. Ledzewicz, H. Maurer, H. Schattler, Optimal combined radio- and anti-angiogenic cancer therapy, *J. Optim. Theory Appl.*, **180** (2019), 321–340. <https://doi.org/10.1007/s10957-018-1426-y>
78. H. Sbeity, R. Younes, Review of optimization methods for cancer chemotherapy treatment planning, *J. Comput. Sci. Syst. Biol.*, **8** (2015), 74–95. <https://doi.org/10.4172/jcsb.1000173>
79. I. Elmouki, S. Saadi, BCG immunotherapy optimization on an isoperimetric optimal control problem for the treatment of superficial bladder cancer, *Int. J. Dyn. Control*, **4** (2016), 339–345. <https://doi.org/10.1007/s40435-014-0106-5>
80. I. Elmouki, S. Saadi, Quadratic and linear controls developing an optimal treatment for the use of BCG immunotherapy in superficial bladder cancer, *Optim. Control Appl. Methods*, **37** (2016), 176–189. <https://doi.org/10.1002/oca.2161>
81. A. Hamdache, I. Elmouki, S. Saadi, Optimal control with an isoperimetric constraint applied to cancer immunotherapy, *Int. J. Comput. Appl. Technol.*, **94** (2014), 31–37. <https://doi.org/10.5120/16421-6073>
82. L. de Pillis, K. R. Fister, W. Gu, T. Head, K. Maples, T. Neal, et al., Optimal control of mixed immunotherapy and chemotherapy of tumors, *J. Biol. Syst.*, **16** (2008), 51–80. <https://doi.org/10.1142/S0218339008002435>

83. J. Zhang, Q. He, D. Mao, C. Wang, L. Huang, M. Wang et al., Efficacy and adverse reaction management of oncolytic viral intervention combined with chemotherapy in patients with liver metastasis of gastrointestinal malignancy, *Front. Oncol.*, **13** (2023), 1159802. <https://doi.org/10.3389/fonc.2023.1159802>
84. X. Cheng, Q. Zhao, X. Xu, W. Guo, H. Gu, R. Zhou, et al., Case report: Extragonadal yolk sac tumors originating from the endometrium and the broad ligament: A case series and literature review, *Front. Oncol.*, **11** (2021), 672434. <https://doi.org/10.3389/fonc.2021.672434>
85. A. Rampen, J. Jongen, I. van Heuvel, M. S. de Boer, P. Sonneveld, M. van den Bent, Bortezomib-induced polyneuropathy, *Neth. J. Med.*, **71** (2013), 128–133.
86. R. Orłowski, T. Stinchcombe, B. Mitchell, T. Shea, A. Baldwin, S. Stahl, et al., Phase I trial of the proteasome inhibitor PS-341 in patients with refractory hematologic malignancies, *J. Clin. Oncol.*, **20** (2002), 4420–4427. <https://doi.org/10.1200/JCO.2002.01.133>
87. M. Mateos, J. S. Miguel, Bortezomib in multiple myeloma, *Best Pract. Res. Clin. Haematol.*, **20** (2007), 701–715. <https://doi.org/10.1016/j.beha.2007.09.003>
88. J. Zhang, Y. Liu, J. Tan, Y. Zhang, C. Wong, Z. Lin, et al., Necroptotic virotherapy of oncolytic alphavirus m1 cooperated with doxorubicin displays promising therapeutic efficacy in TNBC, *Oncogene*, **40** (2021), 4783–4795. <https://doi.org/10.1038/s41388-021-01869-4>
89. J. Sprooten, P. Wijngaert, I. Vanmeerbeerk, S. Martin, P. Vangheluwe, S. Schlenner, et al., Necroptosis in immuno-oncology and cancer immunotherapy, *Cell*, **9** (2020), 1823. <https://doi.org/10.3390/cells9081823>
90. K. R. Fister, J. C. Panetta, Optimal control applied to competing chemotherapeutic cell-kill strategies, *SIAM J. Appl. Math.*, **63** (2003), 1954–1971. <https://doi.org/10.1137/S0036139902413489>
91. L. de Pillis, W. Gu, K. Fister, T. Head, K. Maples, A. Murugan, et al., Chemotherapy for tumors: An analysis of the dynamics and a study of quadratic and linear optimal controls, *Math. Biosci.*, **209** (2007), 292–315. <https://doi.org/10.1016/j.mbs.2006.05.003>
92. S. Sabir, N. Raissi, M. Serhani, Chemotherapy and immunotherapy for tumors: A study of quadratic optimal control, *Int. J. Appl. Comput. Math.*, **6** (2020), 81. <https://doi.org/10.1007/s40819-020-00838-x>
93. S. Sharma, G. P. Samanta, Analysis of the dynamics of a tumor-immune system with chemotherapy and immunotherapy and quadratic optimal control, *Differ. Equations Dyn. Syst.*, **24** (2016), 149–171. <https://doi.org/10.1007/s12591-015-0250-1>
94. G. W. Swan, General applications of optimal control theory in cancer chemotherapy, *Math. Med. Biol.: J. IMA*, **5** (1988), 303–316. <https://doi.org/10.1093/imammb/5.4.303>
95. A. E. Glick, A. Mastroberardino, An optimal control approach for the treatment of solid tumors with angiogenesis inhibitors, *Mathematics*, **5** (2017), 49. <https://doi.org/10.3390/math5040049>
96. L. Pontryagin, *Mathematical Theory of Optimal Processes*, Classics of Soviet Mathematics, Taylor & Francis, 1987.
97. G. Tundo, D. Sbardella, A. Santoro, A. Coletta, F. Oddone, G. Grasso, et al., The proteasome as a druggable target with multiple therapeutic potentialities: Cutting and non-cutting edges, *Pharmacol. Ther.*, **213** (2020), 107579. <https://doi.org/10.1016/j.pharmthera.2020.107579>

98. J. Adams, The development of proteasome inhibitors as anticancer drugs, *Cancer Cell*, **5** (2004), 417–421. [https://doi.org/10.1016/S1535-6108\(04\)00120-5](https://doi.org/10.1016/S1535-6108(04)00120-5)
99. D. Johnson, The ubiquitin-proteasome system: Opportunities for therapeutic intervention in solid tumors, *Endocr. Relat. Cancer*, **22** (2015), T1–T17. <https://doi.org/10.1530/ERC-14-0005>
100. G. Kaplan, C. Torcun, T. Grune, N. Ozer, B. Karademir, Proteasome inhibitors in cancer therapy: Treatment regimen and peripheral neuropathy as a side effect, *Free Radical Biol. Med.*, **103** (2017), 1–13. <https://doi.org/10.1016/j.freeradbiomed.2016.12.007>
101. P. Richardson, B. Barlogie, J. Berenson, S. Singhal, S. Jagannath, D. Irwin, et al., Extended follow-up of a phase ii trial in relapsed, refractory multiple myeloma: Final time-to-event results from the summit trial, *Cancer: Interdiscip. Int. J. Am.*, **106** (2006), 1316–1319. <https://doi.org/10.1002/cncr.21740>
102. T. Lawrence, The nuclear factor NF-kappaB pathway in inflammation, *Cold Spring Harb Perspect Biol.*, **1** (2009), a001651.
103. M. Karin, F. Greten, Nf-kappab: linking inflammation and immunity to cancer development and progression, *Nat. Rev. Immunol.*, **5** (2005), 749–759. <https://doi.org/10.1038/nri1703>
104. S. Marino, I. Hogue, C. Ray, D. Kirschner, A methodology for performing global uncertainty and sensitivity analysis in systems biology, *J. Theor. Biol.*, **254** (2008), 178–196. <https://doi.org/10.1016/j.jtbi.2008.04.011>
105. M. Curran, K. Mckeage, Bortezomib: a review of its use in patients with multiple myeloma, *Drugs*, **69** (2009), 859–888. <https://doi.org/10.2165/00003495-200969070-00006>
106. J. S. Miguel, R. Schlag, N. Khuageva, M. Dimopoulos, O. Shpilberg, M. Kropff, et al., Bortezomib plus melphalan and prednisone for initial treatment of multiple myeloma, *N. Engl. J. Med.*, **359** (2008), 906–917. <https://doi.org/10.1056/NEJMoa0801479>
107. S. Bergqvist, G. Ghosh, E. A. Komives, The IκBα/NF-κB complex has two hot spots, one at either end of the interface, *Protein Sci.*, **17** (2008), 2051–2058. <https://doi.org/10.1110/ps.037481.108>
108. E. Mathes, E. L. O’Dea, A. Hoffmann, G. Ghosh, NF-κB dictates the degradation pathway of IκBα, *EMBO J.*, **27** (2008), 1357–1367. <https://doi.org/10.1038/emboj.2008.73>
109. M. Xin, X. Deng, Nicotine inactivation of the proapoptotic function of bax through phosphorylation, *J. Biol. Chem.*, **280** (2005), 10781–10789. <https://doi.org/10.1074/jbc.M500084200>
110. Q. Wang, W. Chen, X. Xu, B. Li, W. He, M. T. Padilla, et al., RIP1 potentiates BPDE-induced transformation in human bronchial epithelial cells through catalase-mediated suppression of excessive reactive oxygen species, *Carcinogenesis*, **34** (2013), 2119–2128. <https://doi.org/10.1093/carcin/bgt143>
111. D. Leveque, M. Carvalho, F. Maloisel, Clinical pharmacokinetics of bortezomib, *In vivo*, **21** (2007), 273–278.
112. R. Kane, P. Bross, A. Farrell, R. Pazdur, The mean elimination half-life of bortezomib after the first dose ranged from 9–15 hours at doses ranging from 1.45–2.00 mg/m<sup>2</sup> in patients with advanced malignancies, *Oncologist*, **8** (2003), 508–513.
113. T. Lipniacki, P. Paszek, A. Brasier, B. Luxon, M. Kimmel, Mathematical model of NF-kappab regulatory module, *J. Theor. Biol.*, **228** (2004), 195–215. <https://doi.org/10.1016/j.jtbi.2004.01.001>

- 114.E. Lee, D. Boone, S. Chai, S. Libby, M. Chien, J. Lodolce et al., Failure to regulate tnf-induced nf-kappab and cell death responses in a20-deficient mice, *Science*, **289** (2000), 2350–2354. <https://doi.org/10.1126/science.289.5488.2350>
- 115.J. Mothes, D. Busse, B. Kofahl, J. Wolf, Sources of dynamic variability in nf-kb signal transduction: a mechanistic model, *Bioessays*, **37** (2015), 452–462. <https://doi.org/10.1002/bies.201400113>
- 116.X. Xu, X. Wang, W. Hu, A modeled dynamic regulatory network of nf- $\kappa$ b and il-6 mediated by mirna, *Biosystems*, **114** (2013), 214–218. <https://doi.org/10.1016/j.biosystems.2013.09.001>
- 117.R. Kirkland, G. Saavedra, B. Cummings, J. Franklin, Bax regulates production of superoxide in both apoptotic and nonapoptotic neurons: role of caspases, *J. Neurosci.*, **30** (2010), 16114–16127. <https://doi.org/10.1523/JNEUROSCI.2862-10.2010>
- 118.J. Li, T. McQuade, A. Siemer, J. Napetschnig, K. Moriwaki, Y. Hsiao, et al., The rip1/rip3 necrosome forms a functional amyloid signaling complex required for programmed necrosis, *Cell*, **150** (2012), 339–350. <https://doi.org/10.1016/j.cell.2012.06.019>
- 119.J. A. O'donoghue, M. Bardies, T. Wheldon, Relationships between tumor size and curability for uniformly targeted therapy with beta-emitting radionuclides, *J. Nucl. Med.*, **36** (1995), 1902–1909.



AIMS Press

© 2024 the Author(s), licensee AIMS Press. This is an open access article distributed under the terms of the Creative Commons Attribution License (<http://creativecommons.org/licenses/by/4.0>)